



## New cosmogenic nuclide constraints on Late Glacial and Holocene glacier fluctuations in the sub-Antarctic Indian Ocean (Kerguelen Islands, 49°S)

Joanna Charton, Irene Schimmelpfennig, Vincent Jomelli, Regis Braucher, Guillaume Delpech, Pierre-Henri Blard, Deborah Verfaillie, Vincent Favier, V.R. Rinterknecht, Hugues Goosse, et al.

### ► To cite this version:

Joanna Charton, Irene Schimmelpfennig, Vincent Jomelli, Regis Braucher, Guillaume Delpech, et al.. New cosmogenic nuclide constraints on Late Glacial and Holocene glacier fluctuations in the sub-Antarctic Indian Ocean (Kerguelen Islands, 49°S). Quaternary Science Reviews, 2022, 283, pp.107461. 10.1016/j.quascirev.2022.107461 . hal-03625148

**HAL Id: hal-03625148**

**<https://hal.science/hal-03625148>**

Submitted on 30 Mar 2022

**HAL** is a multi-disciplinary open access archive for the deposit and dissemination of scientific research documents, whether they are published or not. The documents may come from teaching and research institutions in France or abroad, or from public or private research centers.

L'archive ouverte pluridisciplinaire **HAL**, est destinée au dépôt et à la diffusion de documents scientifiques de niveau recherche, publiés ou non, émanant des établissements d'enseignement et de recherche français ou étrangers, des laboratoires publics ou privés.

**New cosmogenic nuclide constraints on Late Glacial and Holocene glacier fluctuations  
in the sub-Antarctic Indian Ocean (Kerguelen Islands, 49°S)**

Joanna Charton<sup>a</sup>, Irene Schimmelpfennig<sup>a</sup>, Vincent Jomelli<sup>a</sup>, Guillaume Delpech<sup>b</sup>, Pierre-Henri Blard<sup>c</sup>, Régis Braucher<sup>a</sup>, Deborah Verfaillie<sup>a,d</sup>, Vincent Favier<sup>e</sup>, Vincent Rinterknecht<sup>a</sup>, Hugues Goosse<sup>d</sup>, Xavier Crosta<sup>f</sup>, Léo Chassiot<sup>g</sup>, Léo Martin<sup>h</sup>, Damien Guillaume<sup>i</sup>, Claude Legentil<sup>j</sup>, ASTER Team<sup>a,l</sup>

<sup>a</sup>*Aix Marseille Univ, CNRS, IRD, INRAE, CEREGE, Aix-en-Provence, France*

<sup>b</sup>*Université Paris-Saclay, CNRS, GEOPS - France*

<sup>c</sup>*Université de Lorraine, CNRS, CRPG - France*

<sup>d</sup>*Earth and Life Institute, Université catholique de Louvain, Louvain-la-Neuve, Belgium*

<sup>e</sup>*Institut des Géosciences de l'Environnement, Université Grenoble Alpes, CNRS, Grenoble, France*

<sup>f</sup>*UMR CNRS 5805 EPOC, Université de Bordeaux, France*

<sup>g</sup>*Université Laval, Département de Géographie, Québec, Canada*

<sup>h</sup>*Faculty of Geosciences, Utrecht University, Utrecht, The Netherlands*

<sup>i</sup>*Univ Lyon, UJM-Saint-Etienne, UCBL, ENSL, CNRS, LGL-TPE UMR5276 – France*

<sup>j</sup>*Université Paris 1 Panthéon-Sorbonne, CNRS Laboratoire de Géographie Physique - France*

<sup>l</sup>*ASTER Team: Georges Aumaître, Didier Boulès (†), Karim Keddadouche*

\*Corresponding author: Joanna Charton, [charton@cerege.fr](mailto:charton@cerege.fr)

25

26 Abstract:

27 Cosmogenic nuclide dating of glacial landforms on the Kerguelen Archipelago (49°S, 69°E)  
28 gives the opportunity to study multi-millennial glacier fluctuations within the sub-Antarctic  
29 sector of the Indian Ocean. We here dated such geomorphic features to provide time  
30 constraints over the last 17,000 years using *in situ*-produced  $^{36}\text{Cl}$  in three glacial valleys: Val  
31 Travers valley, Ampere Glacier valley and Arago Glacier valley. For the first time, a  
32 combination of *in situ*-produced  $^{36}\text{Cl}$  and  $^{10}\text{Be}$  dating and  $^{26}\text{Al}/^{10}\text{Be}$  ratios analysis was  
33 performed in the quartz-bearing syenite boulders of the Arago Glacier site. In addition, a  
34 Bayesian approach was computed to obtain a better constraint on moraine dating. Glacial  
35 advances occurred during the Late Glacial at  $16.0 \pm 1.9$  ka and at  $12.9 \pm 1.7$  ka in Val  
36 Travers, and at  $13.6 \pm 1.8$  ka in Arago Glacier valley, probably linked to the Heinrich Stadial  
37 1 and/or Antarctic Cold Reversal events, respectively. This suggests that all glaciers at this  
38 latitude were broadly sensitive to the large-scale climatic signal of the Antarctic Cold  
39 Reversal. So far, no Early nor Mid-Holocene moraines have been found in the glacial valleys  
40 on Kerguelen, indicating that the glaciers had probably receded significantly during these  
41 periods. This is in agreement with previously determined  $^{14}\text{C}$  ages from peat bogs, which  
42 suggest extensive deglaciation during several millennia of the Holocene period. Samples  
43 from glacially-polished bedrock surfaces (ranging from  $\sim 4.4$  ka to  $\sim 14$  ka) at Ampere  
44 Glacier site also suggest that this valley was ice free for several millennia during the  
45 Holocene. Finally, glaciers seem to have re-advanced only during the Late Holocene,  
46 especially within the last millennium, at  $\sim 1$  ka,  $\sim 430$  yr and  $\sim 300$  yr. A comparison of this  
47 new dataset with the available  $^{10}\text{Be}$  ages from other southern mid-latitude regions during the  
48 Holocene allows the identification of three different glacier evolution patterns. We suspect

that variations of Kerguelen glaciers, which are located in the Southern Indian Ocean, were controlled by the combined effects of sea surface temperature related to the variations of the Antarctic Polar Front and fluctuations of precipitation related to long-term variations of the Southern Annular Mode.

Keywords: glacier fluctuations, paleoclimate,  $^{36}\text{Cl}$  CRE dating,  $^{10}\text{Be}$  CRE dating, Late Glacial, Antarctic Cold Reversal, Holocene, southern mid-latitudes, sub-Antarctic, Kerguelen Islands.

## 1. Introduction

Reconstruction of the long-term evolution of glacier fluctuations provides the opportunity to better understand their sensitivity to multi-millennial and -centennial climate change, in particular to the variability of air temperature and precipitation. Cosmic ray exposure (CRE) dating of glacio-geomorphologic formations, such as moraines, erratic boulders and glacially-eroded bedrock, using *in situ*-produced cosmogenic nuclides is particularly suited to reconstruct past glacier chronologies (Balco et al., 2020). Most paleoglacier records in the mid-latitudes of the Southern Hemisphere are based on the well-constrained *in situ*  $^{10}\text{Be}$  dating method applied to quartz-bearing moraine boulders (e.g. Putnam et al., 2012; Reynhout et al., 2019). In only few studies moraine chronologies are established from the less commonly used *in situ*  $^{36}\text{Cl}$  and  $^3\text{He}$  (Eaves et al., 2019; Rudolph et al., 2020). A consistent glacier evolution has been evidenced in various regions of the mid-latitudes of the Southern Hemisphere during the Holocene (11.7 ka - present) with glaciers located in New Zealand (e.g. Putnam et al., 2012), South Georgia (e.g. Bakke et al. 2021) and Patagonia (e.g. Reynhout et al., 2019) experiencing their maximal Holocene extent during the Early Holocene (11.6 – 8 ka), followed by a gradual decrease of glacier extent throughout time. This multi-millennial trend is attributed to the variation in summer insolation (Putnam et al., 2012) and at an intra-millennial scale to variations in precipitation intensity (Reynhout et al., 2019, Bakke et al., 2021). However, two additional contrasting patterns of glacier fluctuations have been observed recently. In the Darwin Cordillera (southernmost Patagonia),

Reynhout et al. (2021) provided the first  $^{10}\text{Be}$  moraine chronology that shows a maximum Holocene extent during the last millennium corroborating the radiocarbon-dating-based results from previous studies by Hall et al. (2019), while on the Antarctic Peninsula, a maximal glacier advance was recorded during the Mid-Holocene (8 – 4 ka; Kaplan et al., 2020).

These asynchronous fluctuation patterns challenge the concept of a homogeneous Holocene glacier evolution within the southern mid-latitudes and raise the question whether regional rather than hemispheric climatic variations have driven glacier behavior during the Holocene. While CRE glacial paleorecords are increasingly numerous in Patagonia and New Zealand, the knowledge on glacier fluctuations in other parts of the southern mid-latitudes remains fragmented. To fill this gap, the Kerguelen Archipelago (49°S, 69°E) provides a precious sentinel in the Southern Indian Ocean to reconstruct glacier evolution (Fig. 1). Indeed, Kerguelen is the largest still glaciated sub-Antarctic archipelago of the southern mid-latitudes (Favier et al., 2016), where several terrestrial moraines are preserved and can be dated. Therefore, establishing a meaningful glacier chronology at Kerguelen is of major interest, as it improves our knowledge of glacier fluctuations at the regional southern mid-latitudes scale within the larger scope of the Southern Hemisphere.

Existing studies on Kerguelen glaciers document their fluctuations from Marine Isotopic Stage 3 (MIS-3; 60 – 25 ka) to the last millennium (section 2.2; Jomelli et al., 2017, 2018; Charton et al., 2020; Verfaillie et al., 2021). However, knowledge of the evolution of glaciers at Kerguelen from the end of the Late Glacial (19.0 – 11.7 ka) to the Late Holocene (4 - 0 ka) remains limited. Several discrete radiocarbon ages from peatland (Frenot et al., 1997) revealed by modern recession of the Ampere Glacier suggest that this glacier was at least as small as it is currently during several millennia of the Holocene. Therefore, the aim of this study is to address the paucity of Late Glacial and Holocene glacier constraints at Kerguelen,

using  $^{36}\text{Cl}$  CRE dating on samples of all lithologies, complemented by  $^{10}\text{Be}$  and  $^{26}\text{Al}$  CRE analyses on quartz-bearing syenite samples. To do so, we targeted glacial landforms whose position and glacial context in the landscape may provide information on Late Glacial and Holocene glacier fluctuations (section 2.3). Based on the combination of these two dating methods and a Bayesian approach explained in section 3, we provide an updated Kerguelen glacier chronology spanning from the Late Glacial to the last millennium (sections 4 and 5.1), which is explored in the context of the other glacier and climate records from the southern mid-latitudes (sections 5.2 and 5.3.).

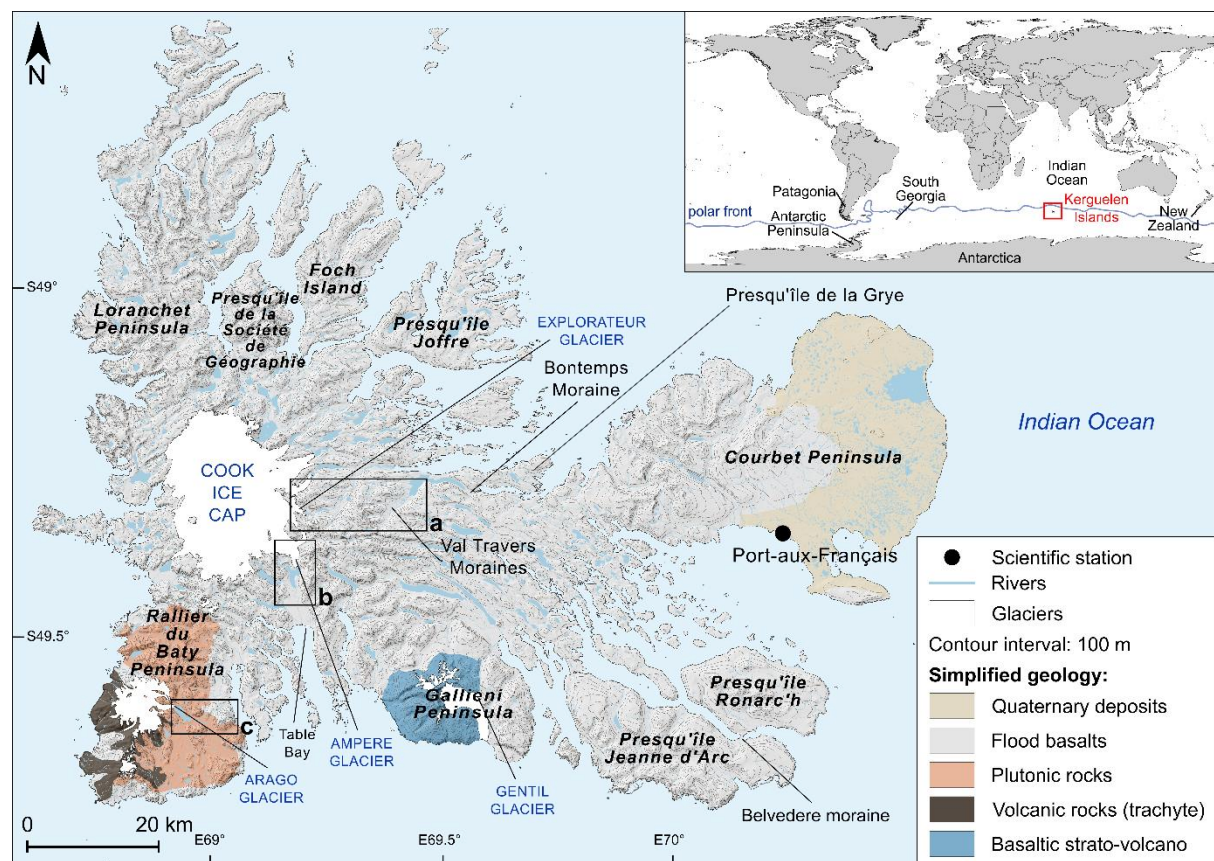


**Figure 1.** Map of the Kerguelen Archipelago with the relevant geology in a simplified form. The inset shows its location in the Southern Indian Ocean. The three study areas are framed in black, **a.** Val Travers site, **b.** Ampere Glacier site, **c.** Arago Glacier site, for which geomorphological maps are presented in Figs. 4, 6 and 7, respectively. (data: Digital

Elevation Model from NASA/METI/AIST/Japan Spacesystems and U.S./Japan ASTER Science Team, 2019; glacier outlines from the GLIMS database (Raup et al., 2007); geological units from Ponthus (2018)).

## 2. Study area and geomorphological setting

The Kerguelen Archipelago is located in the Southern Indian Ocean, with a total surface area of 7215 km<sup>2</sup>. These 30-million-year-old islands constitute the emerging part of the large underwater basaltic Kerguelen Plateau (Giret et al., 2003; Fig. 1). However, the regional geology varies and the basaltic crust is locally intruded by plutonic rocks of various compositions, such as on the Rallier du Baty Peninsula, where a large volcano-plutonic complex contains Qz-bearing syenites, or in the Galliéni Peninsula, which comprises a young volcano-plutonic complex of less than 1 Ma. The eastern part of the Courbet Peninsula is also different and is only characterized by quaternary deposits but no flood basalts (Fig. 1).

### 2.1. Climate setting

Due to its location in the Southern Indian Ocean, the Kerguelen Archipelago is subjected to a subpolar oceanic climate. The related moist and cool air masses, transported by the Southern Westerly Winds (SWW), enabled the formation of ice caps and glaciers. The SWW also drives the Antarctic Circumpolar Current (ACC). The ACC flows eastward between 45°S and 65°S (Sokolov and Rintoul, 2009) and is affected by the bathymetry of the Kerguelen Plateau (46-63°S, 62-85°E). Kerguelen is located in between the sub-Antarctic Front (SAF) at ~ 46°S (Solokov and Rintoul, 2009) and the Antarctic Polar Front (APF) at ~ 50°S (Park et al., 2014). Nowadays, Kerguelen receives an average of 800 mm of precipitation per year and the



mean annual temperature is about 4.5°C at sea level, as recorded daily since 1951 at the scientific station of Port-aux-Français (Courbet Peninsula; Fig. 1). Additional observations have provided information on the spatial variability of the climate in the archipelago (Verfaillie et al., 2015; Favier et al., 2016). In particular, a strong foehn effect has been identified, being responsible for five times more precipitation in the western part than in the eastern part of the archipelago (Verfaillie et al., 2019).

## 2.2. Previous studies on glaciers and their fluctuations at Kerguelen

The western part of the main Kerguelen island, Grande Terre, hosts the warm-based Cook Ice Cap (CIC; 1050 m a.s.l.), which covered ~ 400 km<sup>2</sup> in 2020 (Verfaillie et al., 2021). Several other smaller glaciated areas are also located on the Rallier du Baty Peninsula in the southwest of the archipelago, on the Gallieni Peninsula in the south, and on the Presqu'île de la Société de Géographie north of CIC (Fig. 1).

Previous studies on Kerguelen based on <sup>36</sup>Cl dating of glacial features revealed that glaciers began to retreat at ~41 ka ago (Jomelli et al., 2018). Erratic and bedrock surfaces located farther inland of the island dated to ~29-24 ka suggest that large expanses of ice were still present at that time. Glaciers receded probably until about 15 ka ago. The general glacier recession during the Late Glacial period was interrupted likely during the Antarctic Cold Reversal (ACR; 14.5 -12.9 ka), as indicated by <sup>36</sup>Cl dating of three moraines at different locations – *i.e.* the Bontemps moraine at 13.6 ± 1.5 ka, Belvedere moraine at 15.5 ± 1.8 ka and G1 moraine of Gentil glacier at 14.3 ± 2.3 ka (Jomelli et al., 2017, 2018; Charton et al., 2020). A Late Holocene advance is recorded on the debris-covered Gentil Glacier at 2.62 ± 0.97 ka, located at the base of Mount Ross (the highest summit on Kerguelen; 1850 m a.s.l.) (Charton et al., 2020). Finally, <sup>36</sup>Cl ages from moraines deposited by Ampere Glacier, an outlet glacier of CIC, reveal - albeit with some scatter - the occurrence of at least two

advances of the Ampere Glacier during the last millennium (Jomelli et al., 2017; Verfaillie et al., 2021). One is attributed to the beginning of the Little Ice Age (Solomina et al., 2016), and used to constrain a glaciological model that simulated the extent of the Cook Ice Cap during this period (Verfaillie et al., 2021).

Since the 1960s, glaciers at Kerguelen have experienced dramatic wastage, with the surface area of the CIC expected to disappear by 2100 CE (Verfaillie et al., 2021). This is explained by decreasing precipitation mainly attributed to the high index Southern Annular Mode (SAM+) (Thompson et al., 2011; Verfaillie et al., 2015; Favier et al., 2016) and to the long-term increase in atmospheric temperatures (Verfaillie et al., 2021). Mass and energy balance conducted on the CIC reveals that temperature impacts the precipitation phase and the equilibrium line altitude, through changes in the elevation of the 0°C isotherm and therefore of the rain/snow limit with impacts on both the snow accumulation amount and the glacier surface albedo (Favier et al., 2016).

### 2.3. Study sites and sampling strategy

Three sites hosting datable geomorphological features (i.e. moraines, glacially-polished bedrock and erratics) that are estimated to belong to the Late Glacial and/or the Holocene, based on a comparison with existing data elsewhere on the islands, were chosen: the Val Travers valley, Ampere Glacier and Arago Glacier (Fig. 1). Moraines were labelled with numbers in ascending order from the oldest to the youngest.

The Val Travers site (Fig. 1) is characterized by extended U-shaped valleys that were incised into the basaltic substratum by the eastern outlet glaciers of the CIC. It lies about 10 km upstream of Bontemps Lake (Fig. 4). We sampled the only two preserved terrestrial moraines found in the valley (V1 and V2), which may have been formed by a branch of the Explorateur

203 Glacier (Fig. 4). Four samples (VLT-10, -11, -12, and -13) were taken at 62 m a.s.l from the  
204 V1 moraine ridge, which is located at 14.2 km from the present-day frontal area of the eastern  
205 glaciers of the CIC (Fig. 4). Five moraine boulders (VLT-05, -06, -07, -08, and -09) were  
206 sampled at 73 m a.s.l. on the V2 moraine, which was deposited about 1.5 km upstream of the  
207 V1 moraine (Figs. 2a and 4). Finally, one sample (VLT-04) was extracted from a polished  
208 bedrock surface, located on the right-lateral plateau near Mount A. Gampert at an elevation of  
209 437 m a.s.l. and at a distance of about 9 km downstream of the V1 moraine (Figs. 2a and 4).  
210 All boulders sampled at this site have a basaltic lithology.

211 The Ampere Glacier is a lake-terminating outlet glacier of the CIC, which flows south-east of  
212 the ice cap on the basaltic substratum (Fig. 1). Currently, the Ampere Glacier (67 km<sup>2</sup> in  
213 2011) is 12 km long (Berthier et al., 2009; Verfaillie et al., 2021) with a large proglacial lake.  
214 The Ampere's proglacial margin (9 km long) is characterized by an outwash plain that  
215 reaches Table Bay, with a set of six moraines between about 3.5 and 7 km from the current  
216 ice front (Figs. 1 and 6). Eleven new basaltic samples, i.e. six erratic boulders (MO-03, -04, -  
217 06, -08, -11, and -12) and five bedrock samples (MO-02, -05, -07, -09, and -13) were taken  
218 uphill (between 120 and 290 m a.s.l.) on the southern part of the shore of the Ampere Lake at  
219 distances ranging from 1.5 to 2.8 km from the glacier's snout (Figs. 2b and 6). Each sampled  
220 bedrock surface is paired with at least one erratic (Figs. 2b and 6). These erratic boulders are  
221 aligned in a lateral continuum of the frontal moraine sequence.

222 The south-west part of the archipelago hosts the Rallier du Baty Peninsula (Fig. 1), an  
223 alkaline volcano-plutonic complex, which mostly consists of syenites with rock  
224 crystallization ages ranging from about 12 Ma to 8 Ma (Ponthus et al., 2020). More recent  
225 lava flows, composed of trachytes, are also present, resulting from volcanic activity between  
226 ~1.15 Ma (Dosso et al., 1979) and the last millennium (900-1000 CE) (Guillaume Delpech,

227 personal communication). Rallier du Baty Peninsula is covered by a small ice cap, with  
228 several land-terminating outlet glaciers. Among them, the Arago Glacier, which peaks at  
229 1262 m a.s.l., is a 6 km long lake-terminating glacier and flows down on the eastern slope of  
230 Mont Henri, towards the east into the Larmor valley (Figs. 1 and 7). The only moraine (A1)  
231 so far detected at a distal location (11 km) from the current glacier front, is composed of  
232 syenite boulders. Six syenite samples (RDB-23, -24, -25, -26, -27, and -28) were taken at 72  
233 m a.s.l. on this outermost A1 moraine (Figs. 2c and 7). Closer to the glacier front, a sequence  
234 of four moraines mainly composed of volcanic rocks (trachyte) was identified, but only two  
235 of them (the most distant from the current front) were chosen for dating: A2a and A2b (Fig.  
236 7). They were formed alongside the moraine-dammed lake at about 3 km from the current  
237 glacier front. From the crest of the frontal moraine A2a, four samples (RDB-01, -02, -04, and  
238 -05) were taken at 80 m a.s.l., all being syenites (Fig. 7). Another three samples of trachytic  
239 composition (RDB-15, -17, and -18) were collected from the ridge of the lateral moraine A2b  
240 at 157 m a.s.l. (Figs 2d and 7). In addition, one glacially-polished syenite bedrock sample  
241 (RDB-13) was taken at an average elevation of 60 m a.s.l. on the right-lateral flank of the  
242 valley, located at about 5 km upstream of A1 moraine (Fig. 7).



**Figure 2.** **a.** Photograph of Val Travers site showing V2 moraine and the bedrock surface. **b.** shows a view of Ampere proglacial margin towards Table Bay presenting the sampled paired bedrock surfaces and perched erratic boulders. **c.** and **d.** are photographs of A1 moraine and A2b moraine, respectively, located on Arago Glacier forefield.

### 3. Methods

#### 3.1. Sampling

Sampling was carried out during a field campaign in 2017-2018. In total, 34 samples from glacially-polished bedrock, moraine boulders and erratic boulders were collected (Table 1). A hammer and chisel were used to extract the uppermost 2-3 cm of moraine boulder surfaces, erratic boulders and bedrock (Fig. 2). Particular attention was paid to sample flat and non-weathered surfaces. The geographic coordinates and elevations were recorded with a handheld GPS device and topographic shielding was measured in the field with a clinometer.

#### 3.2. *In situ* cosmogenic nuclide dating

For CRE dating *in situ*  $^{36}\text{Cl}$  is the most suitable cosmogenic nuclide, because Kerguelen's volcanic lithology contains Ca, K, Ti, Fe, and Cl, which are the main target elements for analysis with this method. We also conducted  $^{10}\text{Be}$  measurements on samples that allowed the isolation of sufficient quartz. In addition, we measured  $^{26}\text{Al}$  in these samples with the aim to verify if the sampled surfaces have been affected by some inheritance from the last interglacial (long-term exposure-burial) or by recent exhumation.

### 3.2.1 Chemical procedures

Sample preparation for *in situ*-produced  $^{36}\text{Cl}$ ,  $^{10}\text{Be}$  and  $^{26}\text{Al}$  CRE dating was performed in the “Laboratoire National des Nucléides Cosmogéniques” (LN<sub>2</sub>C) at CEREGE, Aix-en-provence, France. Samples were crushed and sieved to collect the 250-500  $\mu\text{m}$  fraction.

All samples but one (RDB-13) presented in this study were dated with  $^{36}\text{Cl}$ . Basaltic and trachytic whole-rock samples were processed according to routine procedures using a method similar to Schimmelpfennig et al. (2011). The low abundance of phenocrysts in these rocks required the use of the whole-rock fractions for these samples, as in the previous studies in the Kerguelen Islands (Jomelli et al., 2017, 2018; Charton et al., 2020; Verfaillie et al., 2021). Aliquots of bulk rocks were selected for analyses of major and trace element concentrations at the Service d'Analyse des Roches et des Minéraux (SARM, Nancy, France) (Table 2). Major and trace elements are needed to evaluate the contribution of the capture of low-energy neutrons on  $^{35}\text{Cl}$  and the nucleogenic production to the total  $^{36}\text{Cl}$  production. Exposure dating of syenites from Rallier du Baty represented a considerable experimental effort, as they have never been processed before for  $^{36}\text{Cl}$  or other cosmogenic nuclides at the LN<sub>2</sub>C laboratory. All syenite samples are dominated by alkali feldspars (Na and K-rich) with minor amounts of quartz and other magnetic minerals (mainly amphiboles and pyroxenes). Because the feldspars were expected to have low amounts of natural Cl and they are the dominant non-

281 magnetic mineral phase, they were separated for chemical  $^{36}\text{Cl}$  extraction from the magnetic  
282 minerals in the syenite samples (RDB-01, -02, -05, -23, -24, -25, -26, -27 and -28) using a  
283 Frantz magnetic separator. We then leached all samples with a  $\text{HF}/\text{HNO}_3$  (Ultrapur) acid  
284 mixture with the aim to eliminate atmospheric  $^{36}\text{Cl}$  and other potentially Cl-rich mineral  
285 phases (Schimmelpfennig et al., 2009). This step removed ~10-20% of the initial feldspar-  
286 dominated fractions and ~40% of the initial whole rock sample. Another 2 g aliquot of the  
287 rinsed and dried grains for each sample was sent to SARM for major element analyses by  
288 ICP-OES, which provides the concentrations of the target elements (*i.e.* Ca, K, Ti and Fe) for  
289  $^{36}\text{Cl}$  production by spallation and slow muon capture (Table 3). The final dissolution of the  
290 sample grains was performed in a  $\text{HF}/\text{HNO}_3$  (Ultrapur) acid mixture after addition of a  $^{35}\text{Cl}$ -  
291 enriched spike (~99%) for isotope dilution (Ivy-Ochs et al., 2004). In total, 6 chemistry  
292 blanks (Bk 5, Bk 7, Bk 8, Bk 10, Bk 11 and Bk 12) were processed together with the samples  
293 (one with each sample batch, see Table 4 for detailed information). The remaining steps  
294 follow the method presented in Schimmelpfennig et al. (2011). Prior to AMS measurements,  
295  $\text{AgCl}$  targets were pressed into nickel cathodes.  $^{36}\text{Cl}/^{35}\text{Cl}$  and  $^{35}\text{Cl}/^{37}\text{Cl}$  ratio measurements  
296 were performed by Accelerator Mass Spectrometry (AMS) at the French AMS national  
297 facility (ASTER) after normalization to the inhouse standard SM-CL-12, using an assigned  
298 value of  $1.428 (\pm 0.021) \times 10^{-12}$  for the  $^{36}\text{Cl}/^{35}\text{Cl}$  ratio (Merchel et al., 2011) and assuming a  
299 natural ratio of 3.127 for the stable ratio  $^{35}\text{Cl}/^{37}\text{Cl}$ . From these measurements the  $^{36}\text{Cl}$  and Cl  
300 concentrations were calculated, using the principles of isotope dilution and following the  
301 equations in Schimmelpfennig (2009). All concentrations were blank-corrected by  
302 subtracting the number of atoms Cl and  $^{36}\text{Cl}$  of the batch-specific blank from those of the  
303 corresponding samples, respectively (Table 4). An error propagation calculation was  
304 performed following the standard procedures given in Taylor (1997).

305 All syenite samples were inspected for the amount of quartz they contained. Eight samples  
306 were estimated to have at least 1% of quartz, which was isolated from the magnetic minerals  
307 by magnetic separation (using a Frantz magnetic separator) and from K-feldspars by  
308 densimetric separation using heavy liquids. The quartz fraction was leached several times  
309 using a diluted HF acid mixture in an ultrasonic bath to remove any remaining feldspars and  
310 to eliminate atmospheric  $^{10}\text{Be}$  from the quartz grains. Finally, only three samples (RDB-13, -  
311 24 and -27) yielded sufficient amounts of quartz for  $^{10}\text{Be}$  and  $^{26}\text{Al}$  chemical procedures (~12-  
312 52 g from at least 4 kg of crushed rock). As RDB-13 was collected from a quartz-enriched  
313 vein, it yielded the highest amount of quartz (~52 g). The total dissolution of the samples was  
314 then performed in a concentrated HF solution after the addition of 150  $\mu\text{l}$  of an in-house  $^9\text{Be}$   
315 carrier solution ( $3025 \pm 9$  ppm; Merchel et al., 2008). An aliquot of the solution was taken  
316 after complete digestion of the samples to quantify the total Al concentration by ICP-OES  
317 analysis. Due to the presence of high amounts of natural  $^{27}\text{Al}$  in the processed fraction  
318 (probably due to small residues of feldspars), no  $^{27}\text{Al}$  carrier was added to the aliquot.  
319 Beryllium and aluminum were extracted using anion and cation exchange columns and  
320 alkaline precipitation. Afterwards, samples were oxidized at 700°C for 1 hour and the final  
321  $\text{BeO}$  and  $\text{Al}_2\text{O}_3$  were mixed with niobium and silver powders respectively, and loaded into  
322 copper cathodes. AMS measurements of the  $^{10}\text{Be}/^9\text{Be}$  ratios were conducted at the French  
323 national AMS facility (ASTER) (Arnold et al., 2010). Samples were calibrated against the in-  
324 house standard STD-11 ( $^{10}\text{Be}/^9\text{Be} = 1.191 \pm 0.013 \times 10^{-11}$ ; Braucher et al., 2015) and using a  
325  $^{10}\text{Be}$  half-life of  $1.387 (\pm 0.0012) \times 10^6$  years (Chmeleff et al., 2010; Korschinek et al., 2010).  
326 Aluminum measurements were performed against an in-house standard SM-Al-11 with  
327  $^{26}\text{Al}/^{27}\text{Al} = (7.401 \pm 0.064) \times 10^{-12}$  which has been cross-calibrated against the primary  
328 standards certified by a round-robin exercise (Merchel and Bremser, 2004). Analytical  
329 uncertainties include ASTER counting statistics and stability, the latter amounting to ~0.5%



for  $^{10}\text{Be}$  (Arnold et al., 2010).  $^{10}\text{Be}$  measurements were corrected for blank background by subtracting the number of atoms  $^{10}\text{Be}$  of the blank from those of the samples (Table 5).

### 3.2.2. CRE age calculations

The  $^{36}\text{Cl}$  CRE age calculations were performed using the Excel® spreadsheet published by Schimmelpfennig et al. (2009), following the methods used in the previous Kerguelen studies (Jomelli et al., 2017, 2018; Charton et al., 2020; Verfaillie et al., 2021). The calculator takes into account all  $^{36}\text{Cl}$  production reactions (spallation of the target elements Ca, K, Ti and Fe, slow muon capture by Ca and K, capture of cosmogenic low-energy (*i.e.* thermal and epithermal) neutrons by  $^{35}\text{Cl}$  and nucleogenic production) and provides in detail their relative contributions (Supplemental Material Table 1), based on the sea level and high latitude (SLHL) production rates, scaling factors, sample chemical composition (Tables 2 and 3), sample thickness, topographic shielding, and rock formation age (Table 1). The time-invariant “St” scaling (Stone, 2000) was used for the calculation of all samples. As no local production rates exist for the Kerguelen Archipelago, the following  $^{36}\text{Cl}$  SLHL production rates, mostly calibrated at mid-latitude sites and previously applied in Kerguelen, were used for the calculations:  $42.2 \pm 4.8$  atoms of  $^{36}\text{Cl}$  (g Ca) $^{-1}$  yr $^{-1}$  for Ca spallation (Schimmelpfennig et al., 2011),  $148.1 \pm 7.8$  atoms of  $^{36}\text{Cl}$  (g K) $^{-1}$  yr $^{-1}$  for K spallation (Schimmelpfennig et al., 2014),  $13 \pm 3$  atoms of  $^{36}\text{Cl}$  (g Ti) $^{-1}$  yr $^{-1}$  for spallation of Ti (Fink et al., 2000),  $1.9 \pm 0.2$  atoms of  $^{36}\text{Cl}$  (g Fe) $^{-1}$  yr $^{-1}$  for Fe spallation (Stone et al., 2005), and  $696 \pm 185$  neutrons (g air) $^{-1}$  yr $^{-1}$  for the rate of epithermal neutron production from fast neutrons in the atmosphere at the Earth/atmosphere interface (Marrero et al., 2016). We applied a value of  $160 \text{ g cm}^{-2}$  for the high-energy neutron attenuation length and  $2.4 \text{ g cm}^{-3}$  for the bulk rock density. The two  $^{36}\text{Cl}$  production reactions induced by capture of low-energy neutrons on  $^{35}\text{Cl}$  are hard to quantify,

354 as the low-energy neutron flux depends on the rock composition and environmental factors,  
355 such as snow cover and presence of water (Zreda et al., 1993; Phillips et al., 2001;  
356 Schimmelpfennig et al., 2009; Zweck et al., 2013; Dunai et al., 2014). We therefore attributed  
357 a 30% uncertainty to the  $^{36}\text{Cl}$  production from capture of cosmogenic low-energy neutrons by  
358  $^{35}\text{Cl}$  reaction production, based on empirical and model experiments (Zreda et al., 1993;  
359 Schimmelpfennig et al., 2009; Zweck et al., 2013; Dunai et al., 2014; Marrero et al., 2016).  
360 The estimation of the nucleogenic  $^{36}\text{Cl}$  contribution in the spreadsheet follows the  
361 calculations provided by Phillips and Plummer (1996). The nucleogenic  $^{36}\text{Cl}$  production is  
362 induced by low-energy neutron capture on  $^{35}\text{Cl}$ , but in this case the low-energy neutrons  
363 result from spontaneous fission of  $^{238}\text{U}$  and reactions of alpha-particles generated during U  
364 and Th decay. The calculation method further assumes that nucleogenic  $^{36}\text{Cl}$  production starts  
365 with the rock formation (crystallization) and is not preserved during magmatic processes  
366 (Gosse and Phillips, 2001; Schimmelpfennig et al., 2009; Sarikaya et al., 2018; Anjar et al.,  
367 2021). After ~1-2 Ma, nucleogenic  $^{36}\text{Cl}$  production and decay (half-life of  $^{36}\text{Cl}$ : 301 ka) are in  
368 equilibrium, which makes the nucleogenic  $^{36}\text{Cl}$  contribution sensitive to differences in the  
369 formation ages only if they are <1 Ma (Sarikaya et al., 2018). Most rock samples in our  
370 dataset have formation ages that are much older than 1 Ma (Table 1; Guillaume Delpech,  
371 personal communication). The nucleogenic  $^{36}\text{Cl}$  production is therefore in equilibrium with  
372  $^{36}\text{Cl}$  decay. Only samples from a recent lava flow on Arago Glacier site (samples RDB-01, -  
373 02, -04, -05, -15, -17 and -18) have a young formation age of ~10 ka or less (Guillaume  
374 Delpech, personal communication; Table 1), i.e. the nucleogenic  $^{36}\text{Cl}$  contribution is much  
375 lower than in the older samples. Further, calculations of the nucleogenic  $^{36}\text{Cl}$  production in  
376 the spreadsheet developed by Schimmelpfennig et al. (2009) are based on the assumption that  
377 the nucleogenic flux of neutrons is homogenous within the bulk rock. Thus, the bulk rock  
378 composition in U and Th is commonly used to estimate the nucleogenic production of  $^{36}\text{Cl}$  in

our samples. This assumption is valid when dating volcanic material because the fast cooling of the lava commonly induces little crystallization with the sparse occurrence of bigger phenocrysts in the matrix. In the case of Kerguelen, the basalts and trachytes used in this study are mostly aphyric or have a microlitic porphyric microstructure with only a few percent of phenocrysts. On the contrary, the plutonic syenite samples of our dataset have a coarse-grained microstructure and are composed of large crystals (up to centimeter size), frequently including small inclusions of accessory minerals (hundreds of microns or less) with highly variable U and Th concentrations (eg. zircon, monazite). It is therefore plausible that the nucleogenic neutron flux is not homogeneous in the syenites samples due to the occurrence of accessory minerals in some larger crystals. In order to prevent a bias in the estimation of the nucleogenic production for the plutonic samples, we thus used the U and Th compositions of the feldspar-dominated fractions separated instead of the U-Th concentrations of the bulk fraction because the  $^{36}\text{Cl}$  analysis was performed on these feldspar separates. We assign a formal uncertainty of 5% to the nucleogenic  $^{36}\text{Cl}$  production, as to our knowledge no specific investigations have been conducted on the uncertainties inherent to the commonly-used calculation approach. In the Excel® spreadsheet, all uncertainties are propagated throughout to the final  $^{36}\text{Cl}$  exposure age following the standard procedures given in Taylor (1997).

$^{10}\text{Be}$  CRE ages were calculated with the online CREp program (Martin et al., 2017; <http://crep.crpq.cnrs-nancy.fr>) and are listed in Table 5. Scaling to the sample locations was made according to the time-dependent version of the Stone (2000) scaling (Martin et al., 2017), with the ERA40 atmosphere (Uppala et al., 2005) and the atmospheric  $^{10}\text{Be}$ -based VDM geomagnetic database (Muscheler et al., 2005). The production rate used to compute the  $^{10}\text{Be}$  ages is regional “southern mid-latitudes” mean based on three calibration sites located in Patagonia (Kaplan et al., 2011) and New-Zealand (Putnam et al., 2010b), as

available in the online ICE-D dataset (Martin et al., 2017; <http://calibration.ice-d.org/>). Using the Stone time-dependent scaling in CREp, this regional mean  $^{10}\text{Be}$  production rate corresponds to a sea level high latitude (SLHL) value of  $4.05 \pm 0.04$  atoms  $\text{g}^{-1} \text{yr}^{-1}$ . Note that this value is only 1.5% lower than the global average computed with all available worldwide calibration sites (Martin et al., 2017).

No correction was made for snow cover nor denudation for both the  $^{36}\text{Cl}$  and  $^{10}\text{Be}$  age calculations, in line with previously published  $^{36}\text{Cl}$  ages from Kerguelen. Current seasonal snow cover corresponds to a thickness of maximum 10 cm, during durations of about 1.5 months at 90 m a.s.l. and 3 weeks at 35 m a.s.l. (Verfaillie et al. 2015; Favier et al. 2016). Such cover would correspond to a correction lower than 2 % (Delunel et al., 2014) and can hence be safely neglected. Similarly, given the exposure timescale ( $< 20$  ka), the impact of denudation is probably lower than the analytical uncertainties by denudation processes.

The resulting  $^{36}\text{Cl}$  and  $^{10}\text{Be}$  CRE ages are listed in Table 4 and 5 with their inferred  $1 \sigma$  uncertainties (*i.e.* the total uncertainties which take into account the analytical and production rate uncertainties) and their analytical uncertainties in brackets. Surface exposure ages are also plotted and shown in Figs. 4, 6 and 7. In the main text and on the figures, we indicate the individual ages with their total uncertainties, whereas probability density curves of individual ages are presented with analytical uncertainties only to allow internal comparison (Figs. 3, 5 and 9). For a given site, the obtained ages from a single object (moraine, erratic) were compared using a  $\text{Chi}^2$  test, and 95% outliers were then removed (Ward and Wilson, 1978). Then, in line with former Kerguelen studies, we computed the arithmetic mean  $^{36}\text{Cl}$  age for each object (reported with their total uncertainties in Table 4). All exposure ages are expressed in yr until 1 ka, and in ka for older ages.

### 3.3. Bayesian modeling

To reduce the dating uncertainties, we exploited the stratigraphic relationships between the dated glacial objects and applied a Bayesian filter on a part of our  $^{36}\text{Cl}$  moraine age dataset (Cooley et al., 2006; Naveau et al., 2007; Parnell, 2011), following an approach previously developed (Blard et al., 2013; Martin et al., 2018). In practice, we first computed a synthetic probability density function (pdf) for each moraine, summing the individual pdf of all individual  $^{36}\text{Cl}$  ages  $f_{\text{Sample}}$ :

$$f_{\text{Moraine}}(t) = \frac{1}{n} \sum_{i=1}^n f_{\text{Sample}} \quad (1)$$

Then, the pdf of ages of moraines that are in successive stratigraphic order were processed using Bayesian filtering. Including these stratigraphic observations permitted to refine the pdf of both younger and older moraines, considering that a distal moraine is necessarily older than a proximal one (Martin et al., 2018). Filtered pdf,  $f^*$  of older and younger moraines, are computed according to Equations (2) and (3), respectively:

$$f_{\text{Older Moraine}}^*(t) = f_{\text{Older Moraine}}(t) \times \int_0^t f_{\text{Younger Moraine}}(\tau) d\tau \quad (2)$$

$$f_{\text{Younger Moraine}}^*(t) = f_{\text{Younger Moraine}}(t) \times \int_t^\infty f_{\text{Older Moraine}}(\tau) d\tau \quad (3)$$

This filtering is useful to reduce the total dating uncertainties arising from geological dispersions (erosion or inheritance). In practice, the vicinity of the successive moraines of this dataset implied that this filtering was only applied to moraines V1 and V2 of Val Travers (this study; Fig. 3) and moraines M1 and M2 of Ampere ( $^{36}\text{Cl}$  ages were first published in

Jomelli et al. (2017) and Verfaillie et al. (2021); Fig. 5). It was indeed unnecessary to apply this filtering to other moraine couples, because the corresponding  $^{36}\text{Cl}$  ages are too distant.

### 3.4. Review of existing Holocene cosmogenic data

We aim to compare the updated Kerguelen glacial chronologies to those from other southern mid-latitude regions. To address this issue, we focused on studies devoted to alpine glaciers, from the alpine ICE-D database (<http://alpine.ice-d.org/>), which compiles cosmogenic nuclide exposure ages (mostly  $^{10}\text{Be}$ ) from alpine glacier sites around the world. We preferentially target moraine datasets providing direct dating of the main advances of a glacier. Available data from southern mid-latitude glacier chronologies (n=14) were tabulated as follows: (i) moraine mean ages with their inferred internal uncertainties were attributed to one of the subperiods of the Holocene (Early, Mid- or Late Holocene) based on the nominal age and (ii) we only selected the glacial chronologies for which the entire sequence of Holocene moraines in the valley were preserved and dated. After age compilation, we identified patterns according to either the presence or absence of at least one moraine belonging to a specific subperiod in each valley. The results and interpretation of these patterns are presented in Supplementary Material Table 2, 3 and 4 and in Fig 8. The class of data is shown as qualitative histograms. The x-axis of the histograms represents the three sub periods of the Holocene, namely Early Holocene (11.6 - 8 ka), Mid-Holocene (8 - 4 ka) and Late Holocene (4 - 0 ka). The height of the bar represents the qualitative appreciation of the length of the glacier following the stratigraphic principle.

## 4. Results and age interpretation

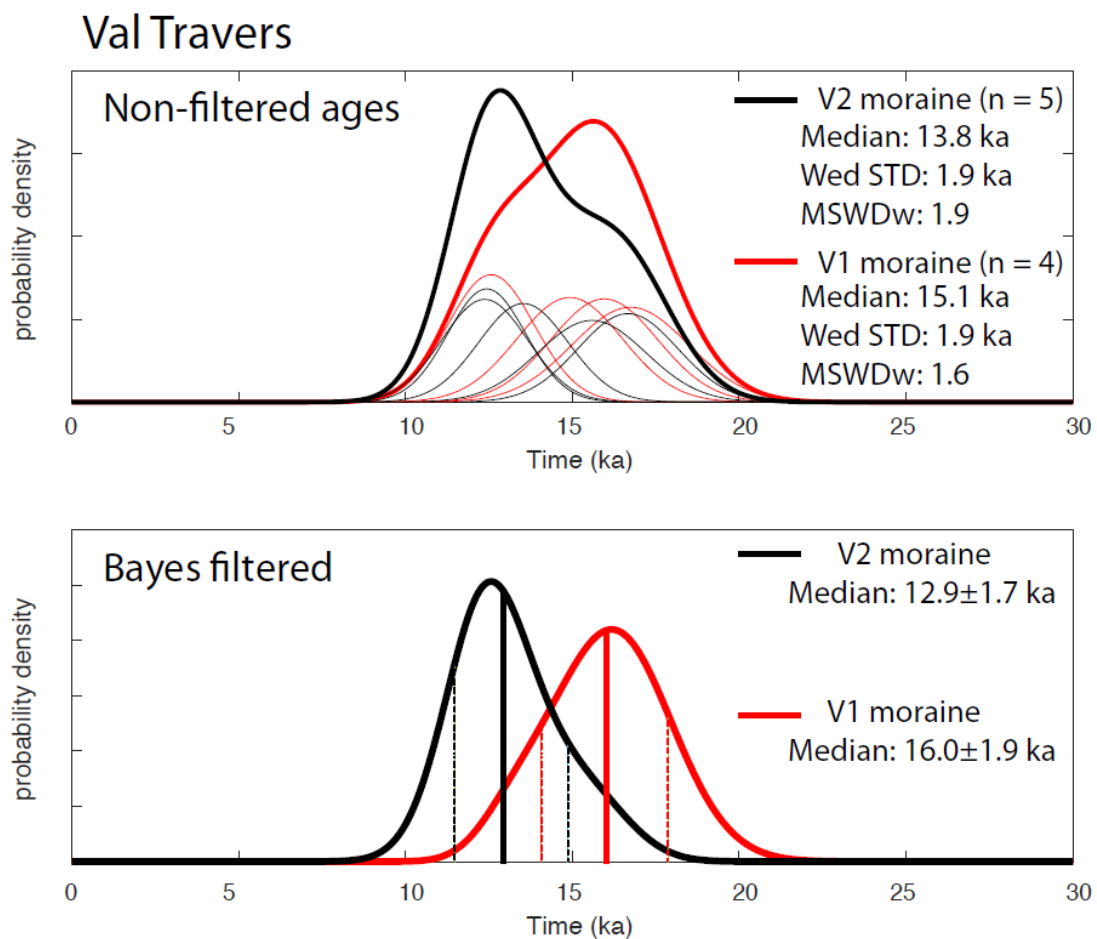
478

479 4.1.  $^{36}\text{Cl}$  ages from Val Travers site (n=10)

480

481 Samples VLT-10, -11, -12 and -13 from V1 moraine give ages of  $12.6 \pm 1.7$  ka,  $16.0 \pm 2.1$  ka,  
482  $16.7 \pm 2.2$  ka and  $14.9 \pm 2.0$  ka respectively and yield a median age of  $16.0 \pm 1.9$  ka after the  
483 Bayesian filtering process, (n=4). (Table 4, Fig. 3, Fig. 4).  $^{36}\text{Cl}$  ages of VLT-05, -06, -07, -08  
484 and -09, collected on V2 moraine are  $15.6 \pm 2.0$  ka,  $12.4 \pm 1.6$  ka,  $12.4 \pm 1.5$  ka,  $16.7 \pm 2.0$  ka  
485 and  $13.5 \pm 1.7$  ka, respectively. The median age and total uncertainty of V2 moraine is  $12.9 \pm$   
486  $1.7$  ka (n = 5) (Table 4, Fig. 3, Fig. 4). The  $^{36}\text{Cl}$  age of VLT-04, which was extracted from a  
487 bedrock atop the U-shaped valley is  $17.3 \pm 2.2$  ka (Table 4, Fig. 4).

488



489

**Figure 3.** Probability plots of  $^{36}\text{Cl}$  boulder CRE ages from V1 (red curves) and V2 (black curves) moraines at Val Travers site before the Bayesian filter (upper panel) and after the Bayesian filter (bottom panel). Individual ages are represented by Gaussian curves in the upper panel, which only include the analytical uncertainties. The summed probability is presented by thick curves. Also shown are the statistical parameters for each landform.

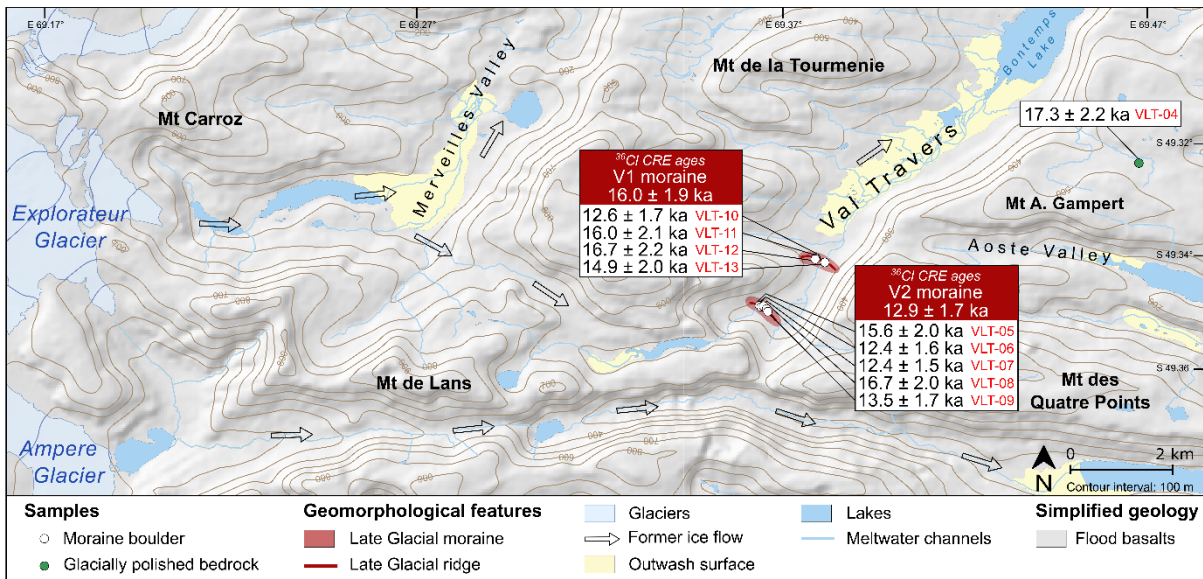
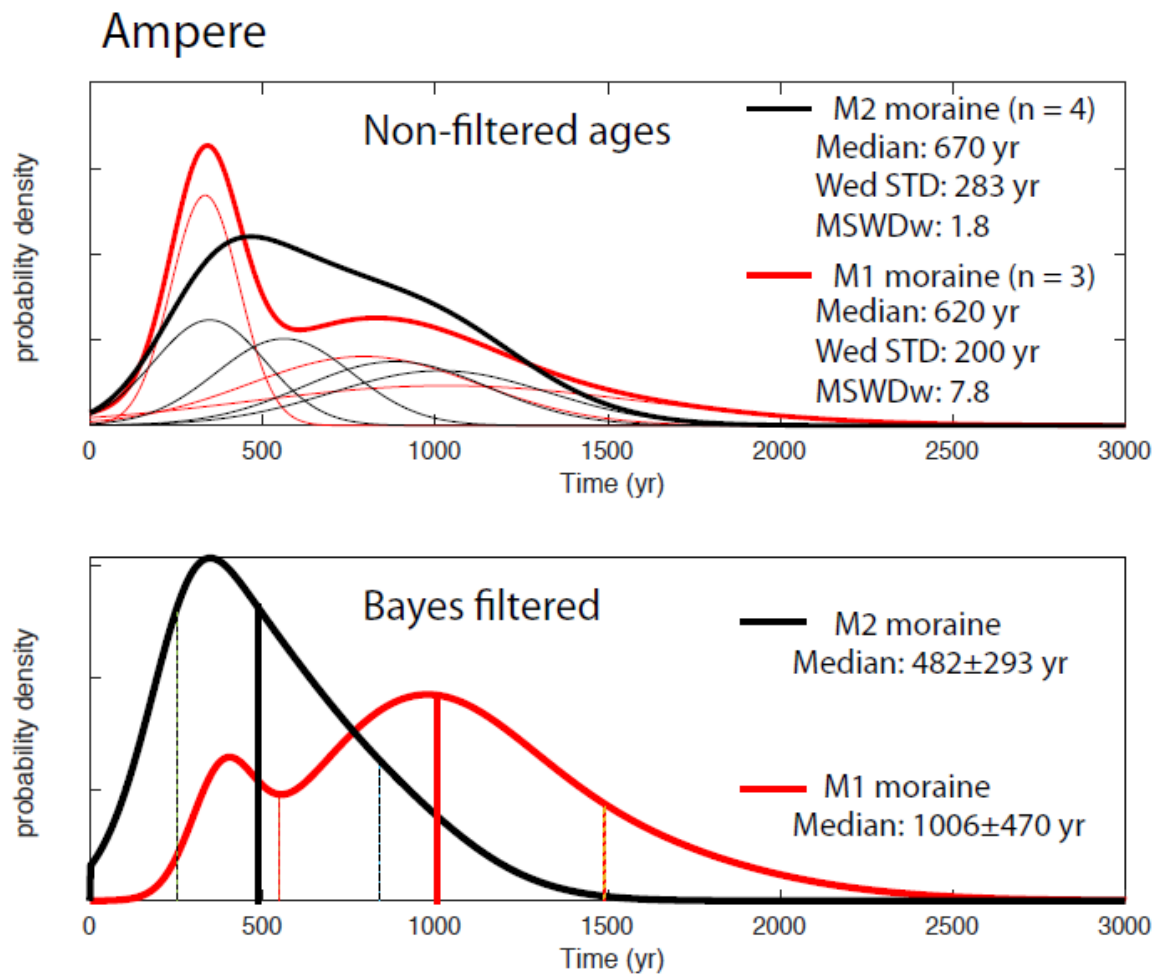


**Figure 4.** Glacial geomorphological map of the Val Travers site. White boxes show the  $^{36}\text{Cl}$  sample ages of moraine and bedrock with their analytical uncertainties. The median ages for moraine groups are shown in colored boxes with their total uncertainties (i.e. standard deviation, analytical and production rate uncertainties).

#### 4.2. $^{36}\text{Cl}$ ages from Ampere Glacier site (n= 11)



The erratic boulder samples associated with bedrock surfaces, MO-12, -11, -04, -03, -08 and -06, yield ages of  $290 \pm 140$  yr,  $870 \pm 180$  yr,  $80 \pm 50$  yr,  $680 \pm 340$  yr,  $620 \pm 170$  yr and  $2.37 \pm 0.38$  ka, respectively (Table 4, Fig. 6). MO-04 and -06 were identified as outliers based on the  $\text{Chi}^2$  test and were therefore excluded from the mean age calculation. MO-04 has an age considered too young probably due to post-depositional rotation or exhumation, whereas the older age of MO-06 is probably affected by inheritance. The remaining samples MO-12, -11, -03 and -06 have a mean arithmetic age of  $610 \pm 250$  yr. The bedrock samples MO-13, -05, -02, -09 and -07 taken from downstream to upstream on the right shore of Ampere Lake yield ages of  $11.3 \pm 1.6$  ka,  $14.0 \pm 1.8$  ka,  $10.1 \pm 1.3$  ka,  $4.43 \pm 0.59$  ka and  $8.9 \pm 1.1$  ka (Table 4, Fig. 6). The interpretation of these ages will be discussed in section 5.1. Individual moraine boulder  $^{36}\text{Cl}$  ages presented in Fig. 6 were first published in Jomelli et al. (2017) and Verfaillie et al. (2021). The weighted means of M1 and M2 moraines and associated total uncertainties gave ages of  $800 \pm 260$  yr and  $580 \pm 310$ , respectively. After the Bayesian filtering process, M1 moraine gives a median age of  $1000 \pm 470$  yr ( $n=3$ ) and M2 moraine gives a median age of  $480 \pm 290$  yr ( $n=4$ ) (Fig. 5).



522

523 **Figure 5.** Probability plots of  $^{36}\text{Cl}$  boulder CRE ages from M1 (red curves) and M2 (black  
 524 curves) moraines at Ampere site ( $^{36}\text{Cl}$  boulder CRE ages were first published in Jomelli et al.  
 525 (2017) and Verfaillie et al. (2021)) before the Bayesian filter (upper panel) and after the  
 526 Bayesian filter (bottom panel). Individual ages are represented by Gaussian curves in the  
 527 upper panel, which only include the analytical uncertainties. The summed probability is  
 528 presented by thick curves. Also shown are the statistical parameters for each landform.

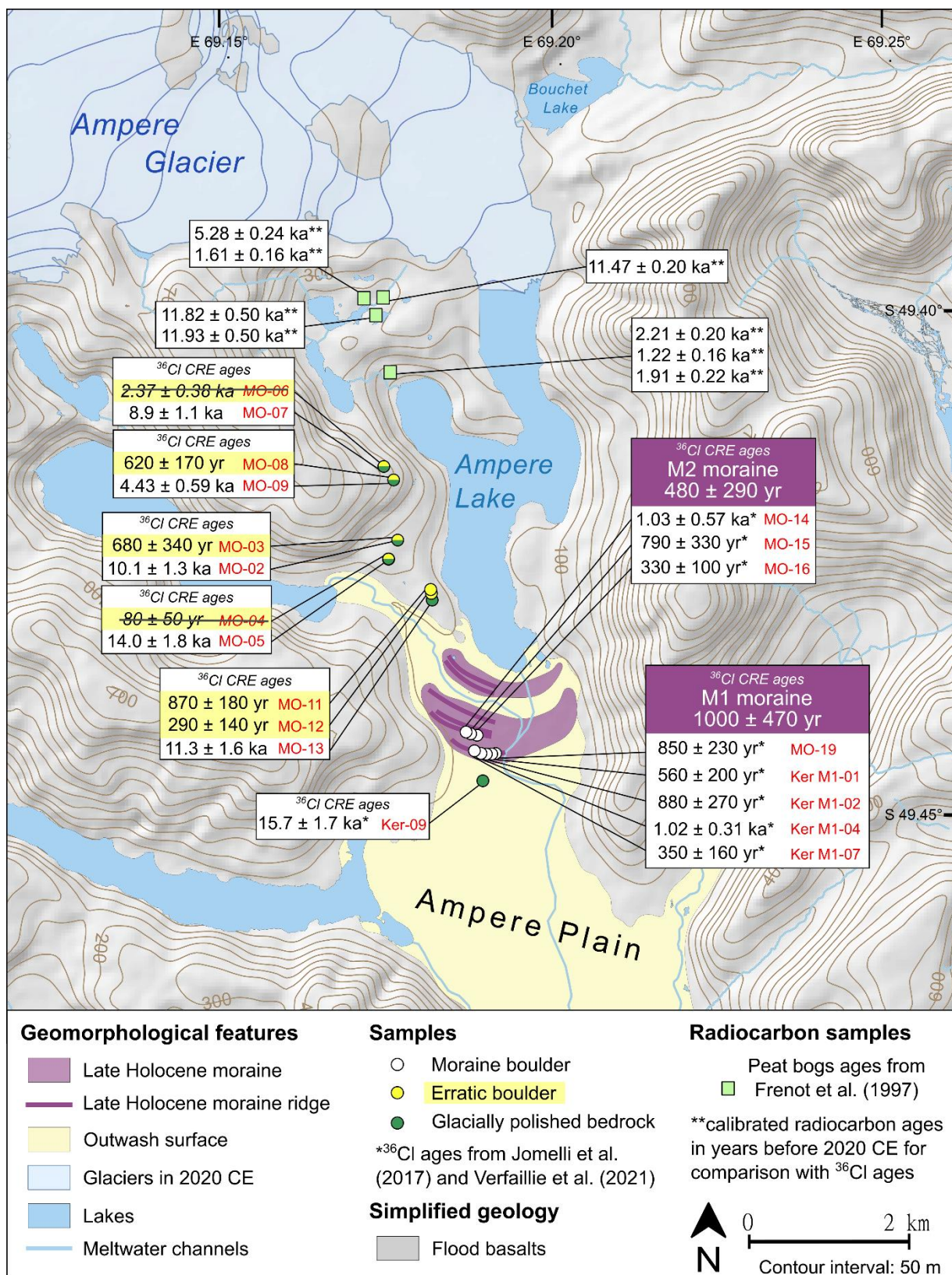


**Figure 6.** Glacial geomorphological map of the Ampere Glacier. White boxes show the  $^{36}\text{Cl}$  sample ages of erratic boulders and bedrock with their inferred analytical uncertainties. Samples written in striked-through italic text are rejected as outliers and therefore excluded

from the discussion. Moraine boulder  $^{36}\text{Cl}$  CRE ages are from Jomelli et al. (2017) and Verfaillie et al. (2021). The median ages for moraine groups are shown in colored boxes with their total uncertainties (i.e. standard deviation, analytical and production rate uncertainties). Radiocarbon ages in cal BP are presented in Jomelli et al. (2017).

#### 4.3. $^{36}\text{Cl}$ ages (n=13), $^{10}\text{Be}$ ages (n=3) and $^{26}\text{Al}/^{10}\text{Be}$ ratios (n=2) from Arago Glacier site

At the Arago Glacier sampling site, we dated three moraines, one bedrock surface and three erratic boulders. The outermost A1 moraine, composed of syenites, was dated using  $^{36}\text{Cl}$  on feldspar separates from all samples, and  $^{10}\text{Be}$  and  $^{26}\text{Al}$  on quartz of two samples. The bedrock surface (RDB-13), which was also sampled from a syenite, was dated only with  $^{10}\text{Be}$  and  $^{26}\text{Al}$  on quartz. Finally, the two innermost moraines A2a-b, composed of trachytes and syenites, were dated with  $^{36}\text{Cl}$  on whole rock and feldspar separates.

The  $^{36}\text{Cl}$  surface exposure ages at the Arago Glacier site range from  $760 \pm 150$  yr to  $15.4 \pm 3.1$  ka (Table 4, Fig. 7) and moraine ages are in agreement with their stratigraphic position. The  $^{36}\text{Cl}$  ages RDB-01, -02, -04 and -05 of the outermost (oldest) A2a moraine are  $760 \pm 150$  yr,  $1.38 \pm 0.23$  ka,  $2.25 \pm 0.44$  ka and  $1.21 \pm 0.23$  ka, respectively. RDB-04 is probably affected by nuclide inheritance and is rejected as an outlier. The arithmetic mean of the remaining ages of A2a moraine and total uncertainty are  $1.12 \pm 0.33$  ka (n = 3). On the innermost (youngest) A2b moraine, samples RDB-15, -17 and -18 give  $^{36}\text{Cl}$  ages of  $480 \pm 120$ ,  $170 \pm 90$ ,  $230 \pm 60$  yr and the moraine has a mean age of  $300 \pm 170$  yr.

Near Les Deux Frères (in between A1 moraine and A2a-b moraine complex; Fig. 7), the bedrock sample RDB-13, collected in syenites upstream of A1 moraine, yields a  $^{10}\text{Be}$  age of  $12.53 \pm 0.46$  ka and a  $^{26}\text{Al}/^{10}\text{Be}$  ratio of  $6.48 \pm 0.64$  (Table 5), which is consistent with the

557  $^{26}\text{Al}/^{10}\text{Be}$  production ratio of 6.75 calculated by Balco and Rovey (2008) and Balco et al.  
558 (2008). This age suggests that this bedrock sample has been continuously exposed at the  
559 surface and does not contain any isotopic inheritance from the last interglacial stadial.

560 Samples RDB-23, -24, -25, -26, -27 and -28, which were collected on the top of the  
561 outermost (oldest) A1 moraine have individual ages of  $13.7 \pm 2.0$  ka,  $14.1 \pm 2.2$  ka,  $15.4 \pm$   
562  $3.1$  ka,  $11.6 \pm 1.7$  ka,  $9.2 \pm 1.4$  ka and  $13.3 \pm 1.6$  ka, respectively. RDB-24 and -27 yield  $^{10}\text{Be}$   
563 ages of  $16.25 \pm 0.83$  and  $11.00 \pm 0.75$  ka, respectively (Table 5, Fig. 7). No statistical  
564 difference can be observed between  $^{10}\text{Be}$  CRE ages and  $^{36}\text{Cl}$  CRE ages of these two samples  
565 (Tables 4 and 5). The  $^{10}\text{Be}$  and  $^{36}\text{Cl}$  CRE ages of sample RDB-27 are both the lowest in the  
566 whole age population and have to be related to the high RDB-27  $^{26}\text{Al}/^{10}\text{Be}$  ratio of  $9.42 \pm$   
567  $1.41$  that may indicate that this surface might have been exposed at depth and then re-expose  
568 at surface when recently exhumed (Akçar et al., 2017). Therefore, both  $^{10}\text{Be}$  and  $^{36}\text{Cl}$  CRE  
569 ages are considered as outliers. The  $^{26}\text{Al}$  measurement of RDB-24 did not yield a meaningful  
570 result probably due to analytical issues and is therefore not considered further. The mean  $^{36}\text{Cl}$   
571 age for the A1 moraine, excluding RDB-27, is  $13.6 \pm 1.8$  ka ( $n = 5$ ).

572



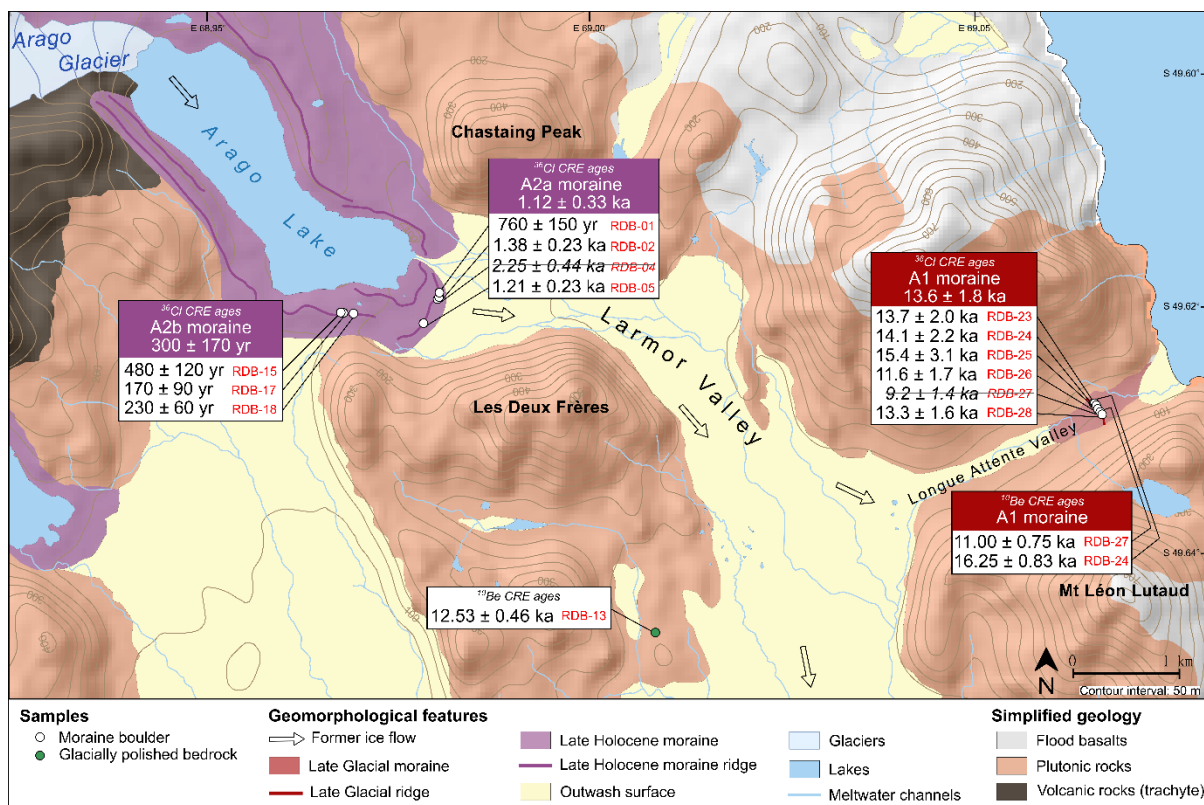


**Figure 7.** Glacial geomorphological map of the Arago Glacier site. White boxes show  $^{36}\text{Cl}$  and  $^{10}\text{Be}$  sample ages of moraine boulders and bedrock with their inferred analytical uncertainties. Samples written in striked-through italic text are rejected as outliers and therefore excluded from the discussion. The arithmetic means for moraine groups are shown in colored boxes with their total uncertainties (i.e. standard deviation, analytical and production rate uncertainties).

## 5. Discussion

### 5.1. Timing of glacier fluctuations at Kerguelen Archipelago since the Late Glacial

Spanning from ~17,000 to ~70 years, this new surface exposure dataset improves our knowledge on the Kerguelen glacier fluctuations during the Late Glacial period and the Holocene (Figs. 4, 6 and 7).

$^{36}\text{Cl}$  dating of a bedrock sample (VLT-04) at an altitude of 437 m a.s.l. at the Val Travers site, suggests that this location became ice free at  $17.3 \pm 2.2$  ka ago (Fig. 4). This finding is consistent with previous ages from erratics at the Presqu'île de la Grye (mean age of  $19.8 \pm 2.2$  ka) located about 10 km east of Val Travers but at an altitude of about 70 m a.s.l. (Jomelli et al., 2017). These results indicate that during the beginning of the Late Glacial period a general deglaciation was occurring (at least in this sector east of CIC).

At the bottom of the adjacent valley, a branch of Explorateur glacier deposited the V1 moraine at  $16.0 \pm 1.9$  ka ago, likely during the Heinrich Stadial 1 (HS1; 17.5–14.7 ka; Rasmussen et al., 2014). However, considering the high uncertainty from this V1 mean moraine age (1.9 ka), it cannot be excluded that this moraine was instead deposited during the beginning of the ACR. In any case, this new data provides another evidence of main glacier extent during this period on the archipelago, as the Belvedere moraine has already been dated to the HS1/ACR period ( $15.5 \pm 1.8$  ka) on the southwest of the archipelago (Jomelli et al., 2018). Upstream in Val Travers another moraine deposition (moraine V2) occurred at  $12.9 \pm 1.7$  ka ago. Within the calculated uncertainties, this moraine age is consistent with previous observations near Presqu'île de la Grye, where the Bontemps moraine was formed northeast of the Val Travers site  $13.6 \pm 1.5$  ka ago by the advance of the Explorateur Glacier (Jomelli et

al., 2018; 2017). On Rallier du Baty Peninsula, the A1 moraine of Arago Glacier may have been formed during the same period at  $13.6 \pm 1.8$  ka ago. Another small debris-covered glacier (Gentil Glacier) located south of the archipelago on the Gallieni Peninsula, also experienced glacial advances that occurred at  $14.3 \pm 2.3$  ka (Charton et al., 2020). All these earlier dated moraines are indistinguishable within the calculated range of uncertainties with the new age of V2 moraines at Val Travers and the A1 moraine at Rallier du Baty peninsula. Altogether, these data suggest that during the phase of deglaciation that had started earlier than about 20 ka, glaciers of the archipelago stagnated or readvanced at least once.

Interestingly, no evidence of Early nor Mid-Holocene glacier extents has been found so far, suggesting that glaciers were smaller at Kerguelen during these periods than they were during the Late Holocene re-advances (Frenot et al., 1997; Jomelli et al., 2017; Charton et al., 2020). These Late-Holocene re-advances are corroborated by new evidence at two sites. One such site is the proglacial margin of Arago Glacier (Fig. 7), where the A2a moraine is dated to the last millennium ( $1.12 \pm 0.33$  ka ago). Several moraine ridges upstream of A2a moraine, including the A2b moraine, that was deposited  $300 \pm 170$  yr ago, attest to further glacier advances or stillstands within the last millennium. Given the absence of moraines between A1 (Late Glacial) and A2a moraines, it is assumed that the glacier generally receded to at least this location between the end of the Late Glacial period and the Late Holocene advance. In addition, the bedrock sample (RDB-13) located on the proglacial margin of the Arago Glacier in between A1 and A2a-b moraines is dated at  $12.53 \pm 0.46$  ka ago, which suggests that this area has been ice free since at least 13 ka.

In Ampere Glacier's forefield, the oldest Holocene advance is recorded by the outermost M1 moraine and, after Bayesian filtering, is now dated at  $1000 \pm 470$  yr ago ( $1110 \pm 470$  CE). A subsequent advance led to the formation of the M2 moraine, which is now dated at  $480 \pm 290$



635 yr ago ( $1590 \pm 290$  CE) (Fig. 6). These findings are complemented by  $^{36}\text{Cl}$  dating of erratic  
636 boulders perched on glacially-polished bedrock surfaces on the right-lateral proglacial margin  
637 of the Ampere Glacier located  $\sim 2\text{--}4$  km upstream and  $\sim 90\text{--}250$  m higher than the M2  
638 moraine. The erratic boulder samples yield a mean age of  $\sim 610$  yr (Fig. 6), which is  
639 indistinguishable from the mean ages of M1 and M2. The prolongation of these aligned  
640 boulders can geometrically be connected with the moraine sequence that M1 and M2 are part  
641 of (Fig. 6). Therefore, it is very likely that they represent the former ice margin that can be  
642 related with the formation of one or several of these last-millennium-moraines. Five of the  
643 erratic boulders are paired with glacially-polished bedrock surface samples, with the goal to  
644 constrain the timing of deglaciation and detect potential periods of successive exposure and  
645 burial, indicated by nuclide inheritance in the bedrock surfaces (e.g. Fabel et al., 2002). The  
646 bedrock surfaces at this location were apparently exposed for durations that range between  
647  $\sim 14$  ka and  $\sim 4$  ka. The apparent  $^{36}\text{Cl}$  CRE ages of the bedrock being systematically older than  
648 those of the erratic boulders (mean age  $\sim 610$  yr), confirm a complex history of bedrock  
649 exposure, meaning that the surfaces contain nuclide inheritance from one or several periods  
650 of exposure that pre-date the last-millennium-advances. Given that the apparent bedrock  
651 exposure durations do not exceed  $\sim 14$  ka and that evidence elsewhere from the Kerguelen  
652 Islands shows large glacier extents still at  $\sim 14$  ka and before, we hypothesize the following  
653 exposure-burial scenario. Substantial ice cover during the last glacial cycle eroded these  
654 locations deeply enough to remove any cosmogenic nuclide inventories that might have  
655 accumulated during previous warm periods; following the retreat from the last large glacier  
656 extents of the ACR (at  $\sim 14$  ka), the sample locations experienced deglaciation and  $^{36}\text{Cl}$   
657 started to accumulate continuously until 1 ka. At this stage, the Ampere Glacier re-advanced  
658 and covered these locations again until (latest)  $\sim 150$  yr ago, as approximately suggested by  
659 the nearby moraine sequence and the erratic boulders located on these bedrock surfaces.

During this last-millennium-ice-cover, the glacier eroded the subglacial bedrock surfaces and thus reduced the  $^{36}\text{Cl}$  inventory accumulated between ~14 ka and 1 ka. Varying erosion rates as a function of topography and related ice velocity led to variable nuclide reduction at the five bedrock surface locations, thus explaining the range of apparent bedrock exposure durations. Following this scenario, a first-order estimate indicates that a uniform subglacial erosion (=abrasion) rate of ~1 mm/yr (corresponding to an abrasion depth of ~85 cm during the ~850 yr of ice cover) can explain the apparent exposure duration of the sample with the lowest  $^{36}\text{Cl}$  inventory (MO-09; ~4.4 ka), whereas sample MO-05 (~14.0 ka) would not have been eroded. Besides abrasion, deep plucking of bedrock is a common subglacial erosion process that can explain variable Holocene cosmogenic nuclide inventories in nearby bedrock surfaces (Rand and Goehring, 2019). Holocene subglacial erosion rates between 0.02 and >1.8 mm/yr have been inferred in crystalline forefields of Alpine glaciers, based on cosmogenic multi-nuclide methods (Goehring et al., 2011; Schimmelpfennig et al., 2022). Rates of between 0 and ~1 mm/yr in volcanic (less hard) rocks and the warm-based glacier setting in Kerguelen seem realistic to explain the apparent variable bedrock exposure durations and the proposed exposure-burial scenario. We consider the possibility of significant  $^{36}\text{Cl}$  inventories inherited from earlier warm periods at these locations unlikely, as no evidence of such warm periods during the last glacial cycle has been provided so far. In addition, significant discrepancies between paired exposure ages of erratics and glacially-polished bedrock elsewhere on Kerguelen may also be expected if nuclide inheritance is a general concern in this setting, like in cold-based glacier sites (Nichols et al., 2019). However, other existing  $^{36}\text{Cl}$  dates of glacially-polished bedrock on the islands are in good agreement with nearby erratics and/or the general deglaciation trend for this region since MIS 3 (Jomelli et al., 2017, 2018). This scenario thus suggests that the new bedrock surfaces investigated in this study were ice-free for most of the Holocene period and provide new

evidence that the Kerguelen glaciers had a little extent during most of the Early and Mid-Holocene.

## 5.2. Comparison with other paleoglacial records within the southern mid-latitude region

The updated  $^{36}\text{Cl}$  dataset consolidates earlier data regarding the Kerguelen glacier chronologies since the Late Glacial, and it also provides new chronological evidence that the Kerguelen glacier behavior followed a different Holocene pattern compared to other regions in the southern mid-latitudes.

Our dataset suggests a possible glacier advance (or stillstand long enough to create a moraine) during HS1 like in Rakaia valley in New Zealand, where glaciers experienced a stillstand at ~16 ka in their global recession trend (Putnam et al., 2013). This is at odds with observations from other southern mid-latitude regions where a global recession of glaciers is generally recorded (e.g. Hall et al., 2013). Our dataset also indicates a glacier advance during the ACR, in agreement with findings from other southern mid-latitude regions (e.g. Putnam et al., 2010a; Pedro et al., 2015; Darvill et al., 2016; Graham et al., 2017). Regarding the Holocene, we performed a review of published moraine CRE ages of glaciers located in Patagonia, New Zealand, Antarctic Peninsula and South Georgia, using the alpine ICE-D database (Balco, 2020) (Fig. 8). Detailed information is available in supplemental material Table 2, 3 and 4. Based on this evaluation, we identified the following three different patterns of glacial evolution in this region of the southern mid-latitudes during the Holocene period (Fig. 8):

- (i) The first pattern, named type-A (glacier sites n=5), corresponds to a decreasing glacial extent throughout the Holocene, evidenced by several

Early, Mid-and Late Holocene moraines dated in numerous glacial valleys. Consequently, glaciers experienced their maximum Holocene advance at the beginning of this period, and then progressively retreated until present-day. Glaciers following the A-type evolution are located in New-Zealand (Putnam et al., 2012), north of 50°S in Patagonia (Reynhout et al., 2019), and South Georgia (Bakke et al., 2021).

(ii) The second pattern, type-B (glacier sites n=5), corresponds to small glacial extents during the Early Holocene, glacier re-advances during the Mid-Holocene and glacier recession during the Late Holocene. These moraines exhibit progressively smaller glacier extents, which are dated to the Mid-and Late Holocene only, and provide evidence of severe glacier retreat during the Early Holocene. Glaciers following this trend are located in Patagonia between ~50°S and 55°S (Kaplan et al., 2016) and in the Antarctic Peninsula (Kaplan et al., 2020 and references therein).

(iii) The last pattern, type-C (glacier sites n=4), is mainly based on what has been documented so far at Kerguelen. According to the currently available estimates, glaciers were smaller throughout the Early to Mid-Holocene than during their maximum Late Holocene extent. Hitherto, the only other location in the Southern Hemisphere where this atypical pattern has been suggested is in southernmost Patagonia (>55°S) (Reynhout et al., 2021 and references therein).



sub-Antarctic Front (SAF) and the purple line is the sub-Tropical Front (STF). Also shown in pink dots are the positions of the marine cores, black dots depict the locations of the ice cores and the single red dot provides the location of the Southern Annular Mode record discussed in section 5.3.

### 5.3. Assessing potential climate drivers of glacier oscillations in Kerguelen Archipelago during the Late Glacial and Holocene

The patterns discussed in section 5.2. provide three regionally contrasting Holocene glacier evolutions within the southern mid-latitude region suggesting complex glacier climatic relationships at a regional scale in the southern mid-latitudes that need to be further explored. Here, we do not address the underlying potential climatic puzzle within the whole southern mid-latitude region but focus on climatic conditions that may have driven glacier fluctuations at Kerguelen (Fig. 9).

We suspect paleoglacier variations at Kerguelen to be strongly impacted by the combined influence of sea surface temperatures (SSTs) variations and precipitation changes related to the position of the westerlies, which is partly driven by the SAM. Since air and sea surface temperatures are significantly correlated at Kerguelen (Favier et al., 2016), paleo SSTs data around Kerguelen should be more relevant for local temperatures, than remote Antarctic ice core records. Moreover, reconstructed SSTs combined with subsurface temperatures from the core MD11-3353 (Fig. 9d and e) located southwest of Kerguelen make it also possible to document latitudinal changes in the position of the oceanic fronts (Civel-Mazens et al., 2021).

As variations of the SAM and the latitudinal gradient of SSTs are not necessarily in phase through time, they may have acted or not in the same direction on paleoglacier behavior. The impacts of negative phases of the SAM (SAM-) (more precipitation) and cold SSTs would

favor a positive mass balance while the effects of a SAM- and warm SSTs would partly compensate for each other.

Below, we explore links between these two climate drivers and glacier patterns throughout the Late Glacial and Holocene. Forcings controlling glacier behavior on Kerguelen remain particularly puzzling for the Late Glacial as precipitation changes and the SAM index for this period remain unknown. Our dataset reveals a general deglaciation trend interrupted by at least one glacier advance or stillstand either during HS1 and/or during the ACR. Assuming an advance or a stillstand during HS1, it would have occurred concomitantly with cold, but warming, atmospheric conditions recorded in Antarctica (Petit et al., 1999; WAIS Divide Project Members, 2013; Fig. 9a and b). If occurring during the ACR, it would have been concordant with the cooling recorded from the Antarctic ice cores (Petit et al., 1999; WAIS Divide Project Members, 2013; Fig. 9a and b) and elsewhere in the Southern Ocean (Pedro et al., 2015). We note that warm SSTs seemingly prevailed at that time, as indicated by core MD11-3353 (Fig. 9d), suggesting that the APF and the SAF were already, and remained, at a more southern latitude. However, the SST record presents very low resolution over the deglaciation, and other SST records suggest the ACR was regionally expressed (Labracherie et al., 1989; Ai et al., 2020; Orme et al., 2020; Civel et al., 2021). The subsurface temperature record in core MD11-3353 conversely shows a plateau during the ACR in agreement with air temperature evolution and glacier standstill. During the ACR, increased moisture input has been reported at the Kerguelen Archipelago, based on multi-proxy analyses of peat sequences (van der Putten et al., 2015). This might be due to a potential northward shift of the SWW during this period and might explain a positive glacier mass balance due to enhanced precipitation. This concept is supported by intensified wet conditions documented from different proxy records in Patagonia (Davies et al., 2020) suggesting that the SWW were

centered at  $\sim 50^{\circ}\text{S}$  during the ACR, while the modern SWW belt lies between  $50^{\circ}\text{S}$  and  $60^{\circ}\text{S}$  (Garreaud et al., 2009).

During the Holocene a reconstruction of precipitation changes attributed to SAM variations offers a good opportunity to analyze the influence of the centennial-to-millennial expression of this climate mode on glacier dynamics at Kerguelen. So far, only one precipitation-SAM reconstruction spanning the Early to Late Holocene exists, and is inferred from the Lago Cipreses non-arboreal pollen (NAP) record in Patagonia ( $51^{\circ}\text{S}$ ) (Moreno et al. 2018; Fig. 9f). According to this record, SAM is mostly characterized by positive-state-like SAM conditions (less precipitation at the latitude of Kerguelen) during the Early Holocene, i.e. from  $\sim 11.5$  to  $\sim 10.2$  ka, and during the so called ‘Early Warm Dry Anomaly’, from  $\sim 9.5$  to 7.5 ka, which is in agreement with warm and dry climate conditions from the Kerguelen Islands inferred from a multi-proxy analyses on a peat record (reconstruction of wind strength, humidity and relative temperature) investigated by van der Putten et al. (2015). In addition, the Holocene trend of reconstructed SSTs (Kauffman et al., 2020) near Kerguelen in the Southern Indian Ocean (shown in Fig. 9c) and southwest of Kerguelen (Civel-Mazens et al., 2021; shown in Fig. 9d) reveals warmer SSTs during the Early Holocene. Altogether dry conditions, in response to pervasive SAM+ like conditions, and rather warm SSTs in the region would explain the relatively small glacier extents at the Kerguelen Archipelago during the Early Holocene.

We notice a cold excursion of SSTs in the Mid-Holocene. Moraines from that time have not yet been identified. Yet, glaciers might have advanced during the Mid-Holocene, but their moraines may have been obliterated by the more extensive Late Holocene glacier advances. However, this potential Mid-Holocene advance may not have lasted long because of the



808 multi-millennial ages of the sampled glacially-polished bedrock, which indicate extensive  
809 deglaciation.

810 During the Late Holocene, negative-state-like SAM conditions increased (Fig. 9f), suggesting  
811 enhanced precipitation, which, combined with rather cold SSTs in the region (Fig. 9c-e),  
812 would have favored glacier re-advance on the Kerguelen Archipelago.

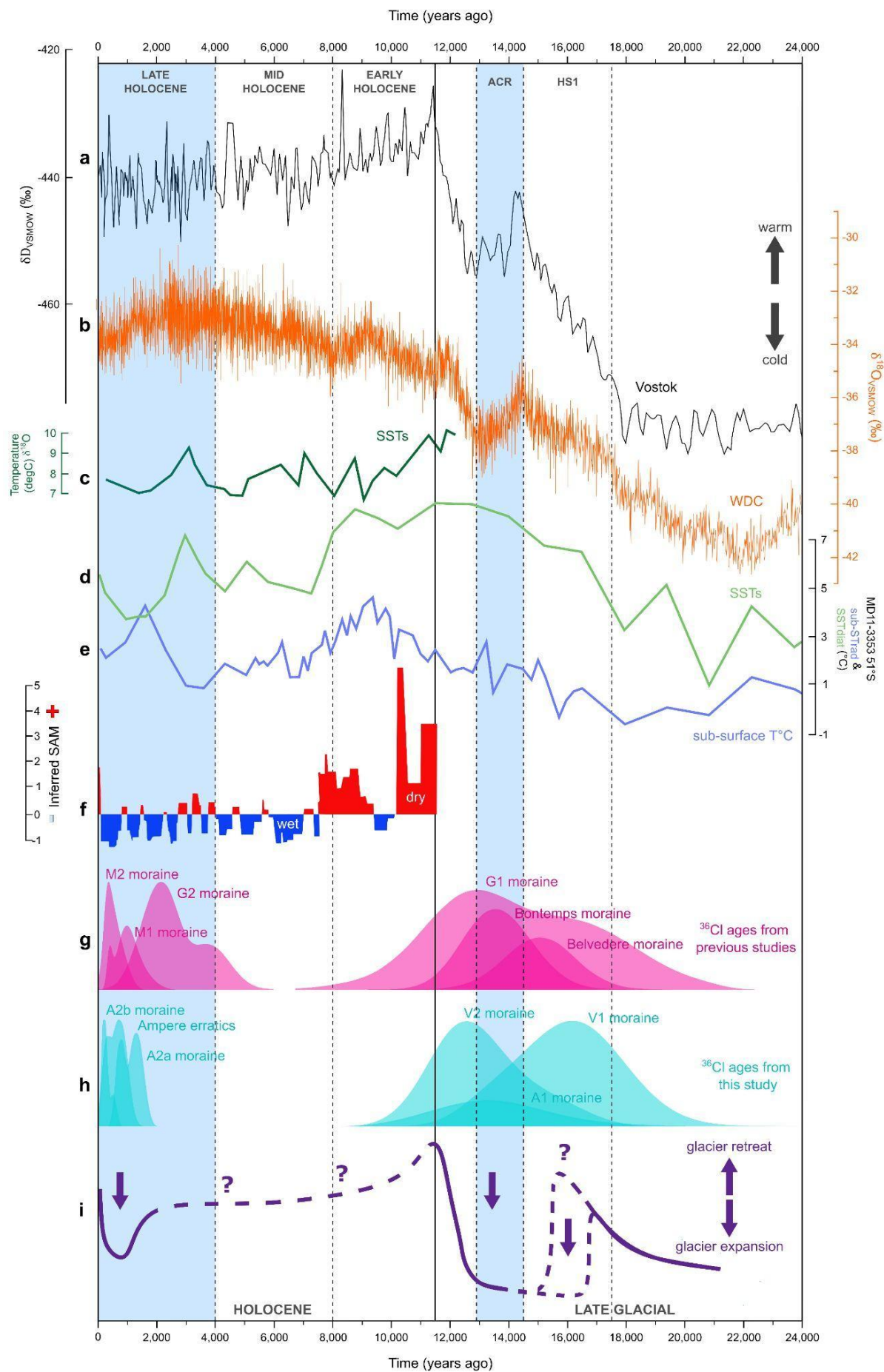


**Figure 9.** Comparison of Kerguelen paleoglacier records with Antarctic and southern mid-latitude climatic proxies (locations are shown in Fig. 8). Proxies for atmospheric temperature fluctuations are **a.**  $\delta D_{VSMOW}$  (black curve) from Vostok (East Antarctica; Petit et al., 1999) and **b.**  $\delta^{18}O_{VSMOW}$  (orange curve) from West Antarctica (WAIS Divide Project Members, 2013). **c.** is the SST reconstruction from  $\delta^{18}O$  on planktonic foraminifera (green curve) from MD84-527 marine core, compiled by Kauffman et al. (2020) but first published by Pichon et al. (1992). **d.** is the reconstructed subsurface temperatures and **e.** the SSTs, both from the MD11-3353 core (51°S; Civel-Mazens et al., 2021). **f.** is the Inferred SAM-like index reconstruction for the Holocene period as shaded boxes (red = positive and blue = negative) from Lago Cipreses non-arboreal pollen in Patagonia (Moreno et al., 2018). Also shown are the  $^{36}Cl$  CRE age probability density distributions with their analytical uncertainties only during the Late Glacial and the Holocene periods from Kerguelen of **g.** previous studies (Jomelli et al., 2017, 2018; Charton et al., 2020; Verfaillie et al., 2021) and **h.** this study. Finally, **i.** is a schematic evolution of Kerguelen glacier extents.

## 6. Conclusion

This study aimed to better constrain the evolution of glaciers on the Kerguelen Archipelago, using *in situ*-produced  $^{36}Cl$  CRE dating from moraine boulders, erratic and glacially-polished bedrock collected on forefields of the Arago Glacier, Ampere Glacier and in the Val Travers Valley. Evidence of a Late Glacial glacier advance at the Val Travers site at ~ 16 ka and ~ 12.9 ka and at the Arago Glacier at ~ 13.6 is provided, which can likely be related to the HS1 and ACR cold spells. While the finding of the HS1 advance is infrequent, the ACR advance is consistent with previous results from other locations on the archipelago, and more

837 generally in the southern mid-latitude region, suggesting that glaciers experienced a broadly  
838 synchronous behavior during the ACR.

839 Early and Mid-Holocene glacio-geomorphic features that are testament to glacier advances  
840 have not yet been found on the archipelago. In addition, CRE dating of paired erratic  
841 boulders (~610 yr) and glacially-polished bedrock surfaces (with exposure duration of up to  
842 14 ka) at the Ampere site indicate that this proglacial margin was ice free for several  
843 millennia during the Holocene period. These results, when combined with previously  
844 published radiocarbon-dated peat ages, suggest that the Ampere Glacier was in a retracted  
845 position during most of the Holocene. The new ages also enable refinement of the glacial  
846 chronology for Kerguelen and reveal new Late Holocene advances, at  $\sim 1.12$  ka and  $\sim 300$  yr  
847 at the Arago Glacier site and at  $\sim 1$  ka and  $\sim 430$  yr at the Ampere Glacier site. These findings  
848 suggest that Kerguelen glaciers retreated significantly after their (large) ACR extents and  
849 were smaller than their last-millennium-extents for most of the Holocene. The data also  
850 indicates that the glaciers only re-advanced again from  $\sim 1$  ka. This implies that any moraines  
851 potentially formed during Early and Mid-Holocene were obliterated by the more extensive  
852 Late Holocene glacier extents.

853 To compare this trend with the glacier evolution in other southern mid-latitude regions, a  
854 review of *in situ* cosmogenic data was performed. Three different glacier patterns were  
855 identified within the southern mid-latitudes, implying that glacier/climate relationships across  
856 this region need further investigations. In the Kerguelen region, a rise in nearby SSTs and a  
857 decrease in precipitation, owing to a latitudinal shift of the SWW could explain the relatively  
858 smaller extent of Kerguelen glaciers during the Early Holocene. On the contrary, decreasing  
859 SSTs and increased precipitation during the Mid- and Late Holocene may have led to glacier  
860 expansion in the case of Kerguelen.

861

862 Author contributions

863 VJ, GD, DV, VF, VR, DG and CL conducted the fieldwork on the islands. JC, IS, VJ and GD  
864 participated in producing the cosmogenic data. GA, DB and KK (ASTER Team) performed  
865 accelerator mass spectrometry measurements. JC, IS, VJ, GD, PHB, RB, LM interpreted the  
866 cosmogenic ages; JC, VJ, IS and PHB prepared the figures. All authors contributed to writing  
867 the paper.

868 Acknowledgments

869 This work has received financial support from the LabEx DynamiTe (ANR-11-LABX-0046)  
870 Les Envahisseurs as part of the 'Investissements d'Avenir' programme. This paper was also  
871 supported by the French INSU LEFE Glacepreker project and by the IPEV Kesaaco 1048  
872 project. The  $^{36}\text{Cl}$ ,  $^{10}\text{Be}$  and  $^{26}\text{Al}$  measurements were performed at the ASTER national  
873 accelerator mass spectrometry facility (CEREGE, Aix-en-Provence) that is supported by the  
874 INSU/CNRS, the ANR through the 'Projets thématiques d'excellence' programme for the  
875 'Equipements d'excellence' ASTER-CEREGE action and IRD. We are very thankful for the  
876 compositional analyses at SARM/CRPG (Nancy, France). We also acknowledge the work of  
877 Fatima Mokadem, Laëtitia Léanni and Valery Guillou, who helped processing data.

878

879

880

881

882

883 References:

884 Ai, X.E., Studer, A.S., Sigman, D.M., Martínez-García, A., Fripiat, F., Thöle, L.M., Michel,  
885 E., Gottschalk, J., Arnold, L., Moretti, S., Schmitt, M., Oleynik, S., Jaccard, S.L., Haug,  
886 G.H., 2020. Southern Ocean upwelling, Earth's obliquity, and glacial-interglacial  
887 atmospheric CO<sub>2</sub> change. *Science*, 370(6522), 1348-1352.  
888 <https://doi.org/10.1126/science.abd2115>.

889 Akçar, N., Ivy-Ochs, S., Alfimov, V., Schlunegger, F., Claude, A., Reber, R., Christl, M.,  
890 Vockenhuber, C., Dehnert, A., Rahn, M., Schluchter, C., 2017. Isochron-burial dating of  
891 glaciofluvial deposits: first results from the Swiss Alps. *Earth Surf. Process. Landforms* 42,  
892 2414–2425.

893 Anjar, J., Akçar, N., Larsen, E.A., Lyså, A., Marrero, S., Mozafari, N., Vockenhuber, C.,  
894 2021. Cosmogenic Exposure Dating (<sup>36</sup>Cl) of Landforms on Jan Mayen, North Atlantic, and  
895 the Effects of Bedrock Formation Age Assumptions on <sup>36</sup>Cl Ages. *Geosciences*, 11, 390.  
896 <https://doi.org/10.3390/geosciences11090390>

897 Ansell, H., 2005. Petrology and geochemistry of the 25 Ma Mt. Marion Dufresne basaltic  
898 section on the Kerguelen Archipelago: constraining the transition from Tholeiitic to Mildly  
899 Alkalic volcanism on a major oceanic island, Master of Science – MSc, University of British  
900 Columbia, Canada. <https://doi.org/10.14288/1.0052331>

901 Arnold, M., Merchel, S., Bourles, D., Braucher, R., Benedetti, L., Finkel, R.C., Aumaître, G.,  
902 Gott Dang, A., Klein, M., 2010. The French accelerator mass spectrometry facility ASTER:  
903 improved performance and developments. *Nucl. Instrum. Methods Phys. Res. B: Beam*

904 Interactions with Materials and Atoms, 268, 1954-1959.  
 905 <https://doi.org/10.1016/j.nimb.2010.02.107>.

906 Bakke, J., Paasche, Ø., Schaefer, J., Timmermann, A., 2021. Long-term demise of sub-  
 907 Antarctic glaciers modulated by the Southern Hemisphere Westerlies. *Sci. Rep.* 11, 8361.  
 908 <https://doi.org/10.1038/s41598-021-87317-5>

909 Balco, G., Rovey, C., W., 2008. An isochron method for cosmogenic-nuclide dating of buried  
 910 soils and sediments. *Am. J. Sci.*, 308 (10) 1083-1114. <https://doi.org/10.2475/10.2008.02>.

911 Balco, G., Stone, J.O., Lifton, N.A., Dunai, T.J., 2008. A complete and easily accessible  
 912 means of calculating surface exposure ages or erosion rates from  $^{10}\text{Be}$  and  $^{26}\text{Al}$   
 913 measurements. *Quat. Geochronol.*, 3(3), 174-195.  
 914 <https://doi.org/10.1016/j.quageo.2007.12.001>.

915 Balco, G., 2020. Technical note: A prototype transparent-middle-layer data management and  
 916 analysis infrastructure for cosmogenic-nuclide exposure dating. *Geochronology Discuss.*, 1–  
 917 10. <https://doi.org/10.5194/gchron-2020-6>

918 Berthier, E., Bris, R. le, Mabileau, L., Testut, L., Rémy, F., 2009. Ice wastage on the  
 919 Kerguelen Islands (49°S, 69°E) between 1963 and 2006. *J. Geophys. Res. Earth Surf.*, 114,  
 920 1–11. <https://doi.org/10.1029/2008JF001192>

921 Blard, P.-H., Braucher, R., Lave, J., Bourles, D., 2013. Cosmogenic  $^{10}\text{Be}$  production rate  
 922 calibrated against  $^3\text{He}$  in the high Tropical Andes (3800-4900 m, 20-22°S). *Earth Planet. Sci.*  
 923 *Lett.* 382, 140-149. <https://doi.org/10.1016/j.epsl.2013.09.010>.

924 Braucher, R., Guillou, V., Bourles, D., Arnold, M., Aumaître, G., Keddadouche, K., Nottoli,  
 925 E., 2015. Preparation of ASTER in-house  $^{10}\text{Be}/^9\text{Be}$  standard solutions. *Nucl. Instrum.*

926 Methods Phys. Res. B: Beam Interactions with Materials and Atoms, 361, 335-340.  
 927 <https://doi.org/10.1016/j.nimb.2015.06.012>

928 Charton, J., Jomelli, V., Schimmelpfennig, I., Verfaillie, D., Favier, V., Mokadem, F.,  
 929 Gilbert, A., Brun, F., Aumaître, G., Bourlès, D.L., Keddadouche, K., 2020. A debris-covered  
 930 glacier at Kerguelen (49°S, 69°E) over the past 15 000 years. *Antarct. Sci.*, 33(1), 103–115.  
 931 <https://doi.org/10.1017/S0954102020000541>.

932 Chmeleff, J., von Blanckenburg, F., Kossert, K., Jakob, D., 2010. Determination of the  $^{10}\text{Be}$   
 933 half-life by multicollector ICP-MS and liquid scintillation counting. *Nucl. Instrum. Methods*  
 934 *Phys. Res. B: Beam Interactions with Materials and Atoms*, 268(2), 192-199.  
 935 <https://doi.org/10.1016/j.nimb.2009.09.012>.

936 Civel-Mazens, M., Crosta, X., Cortese, G., Michel, E., Mazaud, A., Ther, O., Ikehara, M.,  
 937 Itaki, T., 2021. Impact of the Agulhas Return Current on the oceanography of the Kerguelen  
 938 Plateau region, Southern Ocean, over the last 40 kyrs. *Quat. Sci. Rev.*, 251, 106711.  
 939 <https://doi.org/10.1016/j.quascirev.2020.106711>

940 Cooley, D., Naveau, P., Jomelli, V., Rabatel, A., Grancher, D., 2006. A bayesian hierarchical  
 941 extreme value model for lichenometry. *Environmetrics*, 17, 555-574.

942 Darvill, C.M., Bentley, M.J., Stokes, C.R., Shulmeister, J., 2016. The timing and cause of  
 943 glacial advances in the southern mid-latitudes during the last glacial cycle based on a  
 944 synthesis of exposure ages from Patagonia and New Zealand. *Quat. Sci. Rev.*, 149, 200–214.  
 945 <https://doi.org/10.1016/j.quascirev.2016.07.024>

946 Davies, B.J., Darvill, C.M., Lovell, H., Bendle, J.M., Dowdeswell, J.A., Fabel, D., García,  
 947 J.L., Geiger, A., Glasser, N.F., Gheorghiu, D.M., Harrison, S., Hein, A.S., Kaplan, M.R.,  
 948 Martin, J.R.V., Mendelova, M., Palmer, A., Pelto, M., Rodés, Á., Sagredo, E.A., Smedley,



949 R.K., Smellie, J.L., Thorndycraft, V.R., 2020. The evolution of the Patagonian Ice Sheet from  
 950 35 ka to the present day (PATICE). *Earth-Sci. Rev.*, 204, 103152.  
 951 <https://doi.org/10.1016/j.earscirev.2020.103152>

952 Delunel, R., Bourlès, D.L., van der Beek, P.A., Schlunegger, F., Leya, I., Masarik, J., Paquet,  
 953 E., 2014. Snow shielding factors for cosmogenic nuclide dating inferred from long-term  
 954 neutron detector monitoring. *Quat. Geochronol.*, 24, 16-26.  
 955 <https://doi.org/10.1016/j.quageo.2014.07.003>.

956 Dosso, L., Vidal, P., Cantagrel, J-M., Lameyre, J., Marot, A., Zimine, S., 1979. Kerguelen:  
 957 continental fragment or oceanic island: petrology and isotopic geochemistry evidence. *Earth*  
 958 *Planet. Sci. Lett.*, 43, 46-60.

959

960 Dunai, T.J., Binnie, S.A., Hein, A.S., Paling, S.M., 2014. The effects of a hydrogen-rich  
 961 ground cover on cosmogenic thermal neutrons: Implications for exposure dating. *Quat.*  
 962 *Geochronol.*, 22, 183–191. <https://doi.org/10.1016/j.quageo.2013.01.001>

963 Favier, V., Verfaillie, D., Berthier, E., Menegoz, M., Jomelli, V., Kay, J.E., Ducret, L.,  
 964 Malbêteau, Y., Brunstein, D., Gallée, H., Park, Y.H., Rinterknecht, V., 2016. Atmospheric  
 965 drying as the main driver of dramatic glacier wastage in the southern Indian Ocean. *Sci. Rep.*,  
 966 6, 1–12. <https://doi.org/10.1038/srep3239>

967 Fink, D., Vogt, S., Hotchkis, M., 2000. Cross-sections for  $^{36}\text{Cl}$  from Ti at  $E_p = 35\text{-}150\text{ MeV}$ :  
 968 Applications to in-situ exposure dating. *Nucl. Instrum. Methods Phys. Res. B: Beam*  
 969 *Interactions with Materials and Atoms*, 172, 861–866. <https://doi.org/10.1016/S0168->  
 970 [583X\(00\)00200-7](https://doi.org/10.1016/S0168-583X(00)00200-7).

971 Frenot, Y., Gloaguen, J.C., van de Vijver, B., Beyens, L., 1997. Datation de quelques  
 972 sediments tourbeux holocènes et oscillations glaciaires aux îles Kerguelen. *Comptes Rendus*  
 973 *l'Academie Sci.* 320, 567–573. [https://doi.org/10.1016/S0764-4469\(97\)84712-9](https://doi.org/10.1016/S0764-4469(97)84712-9)

974 Garreaud, R.D., Vuille, M., Compagnucci, R., Marengo, J., 2009. Present-day south  
 975 American climate. *Palaeogeogr. Palaeoclimatol. Palaeoecol.*, 281, 180-195.

976 Giret, A., Weis, D., Grégoire, M., Mattielli, N., Moine, B., Michon, G., Scoates, J., Tourpin,  
 977 S., Delpech, G., Gerbe, M.-C., Doucet, S., Ethien, R., Cottin, J.-Y., 2003. L'archipel des  
 978 Kerguelen: les plus vieilles îles dans le plus jeune océan. *Géologues*, 15–23.

979 Goehring, B.M., Schaefer, J.M., Schluechter, C., Lifton, N.A., Finkel, R.C., Jull, A.J.T.,  
 980 Akçar, N., Alley, R.B., 2011. The Rhone Glacier was smaller than today for most of the  
 981 Holocene. *Geology*, 39(7), 679–682. <https://doi.org/10.1130/G32145.1>.

982 Gosse, J.C., Phillips, F.M., 2001. Terrestrial in situ cosmogenic nuclides: theory and  
 983 application. *Quat. Sci. Rev.* 20, 14, 1475-1560. [https://doi.org/10.1016/S0277-](https://doi.org/10.1016/S0277-3791(00)00171-2)  
 984 [3791\(00\)00171-2](https://doi.org/10.1016/S0277-3791(00)00171-2).

985 Graham, A.G.C., Kuhn, G., Meisel, O., Hillenbrand, C.D., Hodgson, D.A., Ehrmann, W.,  
 986 Wacker, L., Wintersteller, P., dos Santos Ferreira, C., Römer, M., White, D., Bohrmann, G.,  
 987 2017. Major advance of South Georgia glaciers during the Antarctic Cold Reversal following  
 988 extensive sub-Antarctic glaciation. *Nat. Commun.* 8, 1-15.  
 989 <https://doi.org/10.1038/ncomms14798>.

990 Hall, B.L., Porter, C.T., Denton, G.H., Lowell, T.V., Bromley, G.R.M., 2013. Extensive  
 991 recession of Cordillera Darwin glaciers in southernmost South America during Heinrich  
 992 Stadial 1. *Quat. Sci. Rev.*, 62, 49-55. <https://doi.org/10.1016/j.quascirev.2012.11.026>.

993 Hall, B.L., Lowell, T.V., Bromley, G.R.M., Denton, G.H., Putnam, A.E., 2019. Holocene  
 994 glacier fluctuations on the northern flank of Cordillera Darwin, southernmost South America.  
 995 Quat. Sci. Rev. 222, 105904 <https://doi.org/10.1016/j.quascirev.2019.105904>.

996 Ivy-Ochs, S., Synal, H.A., Roth, C., Schaller, M., 2004. Initial results from isotope dilution  
 997 for Cl and  $^{36}\text{Cl}$  measurements at the PSI/ETH Zurich AMS facility. Nucl. Instrum. Methods  
 998 Phys. Res. B: Beam Interactions with Materials and Atoms, 223–224, 623–627.  
 999 <https://doi.org/10.1016/j.nimb.2004.04.115>.

1000 Jomelli, V., Mokadem, F., Schimmelpfennig, I., Chapron, E., Rinterknecht, V., Favier, V.,  
 1001 Verfaillie, D., Brunstein, D., Legentil, C., Michel, E., Swingedouw, D., Jaouen, A., Aumaitre,  
 1002 G., Bourlès, D.L., Keddadouche, K., 2017. Sub-Antarctic glacier extensions in the Kerguelen  
 1003 region (49°S, Indian Ocean) over the past 24,000 years constrained by  $^{36}\text{Cl}$  moraine dating.  
 1004 Quat. Sci. Rev. 162, 128–144. <https://doi.org/10.1016/j.quascirev.2017.03.010>

1005 Jomelli, V., Schimmelpfennig, I., Favier, V., Mokadem, F., Landais, A., Rinterknecht, V.,  
 1006 Brunstein, D., Verfaillie, D., Legentil, C., Aumaitre, G., Bourlès, D.L., Keddadouche, K.,  
 1007 2018. Glacier extent in sub-Antarctic Kerguelen archipelago from MIS 3 period: Evidence  
 1008 from  $^{36}\text{Cl}$  dating. Quat. Sci. Rev. 183, 110–123.  
 1009 <https://doi.org/10.1016/j.quascirev.2018.01.008>

1010 Kaplan, M.R., Strelin, J.A., Schaefer, J.M., Denton, G.H., Finkel, R.C., Schwartz, R.,  
 1011 Putnam, A.E., Vandergoes, M.J., Goehring, B.M., Travis, S.G., 2011. In-situ cosmogenic  
 1012  $^{10}\text{Be}$  production rate at Lago Argentino, Patagonia: implications for late-glacial climate  
 1013 chronology. Earth Planet Sci. Lett. 309 (1-2), 21–32. [https://](https://doi.org/10.1016/j.epsl.2011.06.018)  
 1014 [doi.org/10.1016/j.epsl.2011.06.018](https://doi.org/10.1016/j.epsl.2011.06.018).

1015 Kaplan, M.R., Schaefer, J.M., Strelin, J.A., Denton, G.H., Anderson, R.F., Vandergoes, M.J.,  
 1016 Finkel, R.C., Schwartz, R., Travis, S.G., Garcia, J.L., Martini, M.A., Nielsen, S.H.H., 2016.  
 1017 Patagonian and southern South Atlantic view of Holocene climate. *Quat. Sci. Rev.* 141, 112–  
 1018 125. <https://doi.org/10.1016/j.quascirev.2016.03.014>  
  
 1019 Kaplan, M.R., Strelin, J.A., Schaefer, J.M., Peltier, C., Martini, M.A., Flores, E., Winckler,  
 1020 G., Schwartz, R., 2020. Holocene glacier behavior around the northern Antarctic Peninsula  
 1021 and possible causes. *Earth Planet. Sci. Lett.* 534, 116077.  
 1022 <https://doi.org/10.1016/j.epsl.2020.116077>  
  
 1023 Kaufman, D.S., McKay, N.P., Routson, C.C., Erb, M., Davis, B.A.S., Heiri, O., Jaccard, S.,  
 1024 Tierney, J.E., Dätwyler, C., Axford, Y., Brussel, T., Cartapanis, O., Chase, B.M., Dawson,  
 1025 A., de Vernal, A., Engels, S., Jonkers, L., Marsicek, J., Moffa-Sánchez, P., Morrill, C., Orsi,  
 1026 A., Rehfeld, K., Saunders, K., Sommer, P.S., Thomas, E., Tonello, M., Tóth, M., Vachula, R.,  
 1027 Andreev, A., Bertrand, S., Biskaborn, B., Bringué, M., Brooks, S., Caniupán, M., Chevalier,  
 1028 M., Cwynar, L., Emile-Geay, J., Fegyveresi, J., Feurdean, A., Finsinger, W., Fortin, M.-C.,  
 1029 Foster, L., Fox, M., Gajewski, K., Grosjean, M., Hausmann, S., Heinrichs, M., Holmes, N.,  
 1030 Ilyashuk, B., Ilyashuk, E., Juggins, S., Khider, D., Koinig, K., Langdon, P., Larocque-Tobler,  
 1031 I., Li, J., Lotter, A., Luoto, T., Mackay, A., Magyari, E., Malevich, S., Mark, B., Massaferrero,  
 1032 J., Montade, V., Nazarova, L., Novenko, E., Pařil, P., Pearson, E., Peros, M., Pienitz, R.,  
 1033 Płóciennik, M., Porinchu, D., Potito, A., Rees, A., Reinemann, S., Roberts, S., Rolland, N.,  
 1034 Salonen, S., Self, A., Seppä, H., Shala, S., St-Jacques, J.-M., Stenni, B., Syrykh, L., Tarrats,  
 1035 P., Taylor, K., van den Bos, V., Velle, G., Wahl, E., Walker, I., Wilmshurst, J., Zhang, E.,  
 1036 Zhilich, S., 2020. A global database of Holocene paleotemperature records. *Sci. Data*, 7, 1–  
 1037 34. <https://doi.org/10.1038/s41597-020-0445-3>

1038 Korschinek, G., Bergmaier, A., Faestermann, T., Gerstmann, U.C., Knie, K., Rugel, G.,  
 1039 Wallner, A., Dillmann, I., Dollinger, G., von Gostomski, C.L., Kossert, K., Maiti, M.,  
 1040 Poutivtsev, M., Remmert, A., 2010. A new value for the half-life of  $^{10}\text{Be}$  by Heavy-Ion  
 1041 Elastic Recoil Detection and liquid scintillation counting. Nucl. Instrum. Methods Phys. Res.  
 1042 B: Beam Interactions with Materials and Atoms, 268(2), 187–191.  
 1043 <https://doi.org/10.1016/j.nimb.2009.09.020>.  
 1044 Labracherie, M., Labeyrie, L.D., Duprat, J., Bard, E., Arnold, M., Pichon, J.-J., Duplessy, J.-  
 1045 C., 1989. The Last Deglaciation in the Southern Ocean. Paleoceanogr. Paleoclimatol., 4(6),  
 1046 629–638. <https://doi.org/10.1029/PA004i006p00629>.  
 1047 Marrero, S.M., Phillips, F.M., Caffee, M.W., Gosse, J.C., 2016. CRONUS-Earth cosmogenic  
 1048  $^{36}\text{Cl}$  calibration. Quat. Geochronol., 31, 199–219.  
 1049 <https://doi.org/10.1016/j.quageo.2015.10.002>.  
 1050 Martin, L., Blard, P.-H., Balco, G., Lave, J., Delunel, R., Lifton, N., Laurent, V., 2017. The  
 1051 CREp program and the ICE-D production rate calibration database: a fully parameterizable  
 1052 and updated online tool to compute cosmic-ray exposure ages. Quat. Geochronol., 38 (25-4).  
 1053 <https://doi.org/10.1016/j.quageo.2016.11.006>.  
 1054 Martin, L., Blard, P.-H., Lavé, J., Condom, T., Premaillon, M., Jomelli, V., Brunstein, D.,  
 1055 Lupker, M., Charreau, J., Mariotti, V., Tibari, B., ASTER Team, Davy, E., 2018. Lake Tauca  
 1056 Highstand (Heinrich Stadial 1) driven by a southward shift of the Bolivian High. Sci. Adv., 4,  
 1057 1–10. <https://doi.org/10.1126/sciadv.aar2514>.  
 1058 Merchel, S., Bremser, W., 2004 First international  $^{26}\text{Al}$  interlaboratory comparison - Part I.  
 1059 Nuclear Instruments and Methods in Physics Research, Section B: Beam Interactions with  
 1060 Materials and Atoms 223–224, 393–400. <https://doi.org/10.1016/j.nimb.2004.04.076>.

1061 Merchel, S., Arnold, M., Aumaître, G., Benedetti, L., Bourlès, D.L., Braucher, R., Alfimov,  
 1062 V., Freeman, S.P.H.T., Steier, P., Wallner, A., 2008. Towards more precise  $^{10}\text{Be}$  and  $^{36}\text{Cl}$   
 1063 data from measurements at the 10–14 level: Influence of sample preparation. Nucl. Instrum.  
 1064 Methods Phys. Res. B: Beam Interactions with Materials and Atoms, 266(22), 4921–4926.  
 1065 <https://doi.org/10.1016/j.nimb.2008.07.031>.

1066 Merchel, S., Bremser, W., Alfimov, V., Arnold, M., Aumaître, G., Benedetti, L., Bourlès,  
 1067 D.L., Caffee, M., Fifield, L.K., Finkel, R.C., Freeman, S.P.H.T., Martschini, M., Matsushi,  
 1068 Y., Rood, D.H., Sasa, K., Steier, P., Takahashi, T., Tamari, M., Tims, S.G., Tosaki, Y.,  
 1069 Wilcken, K.M., Xu, S., 2011. Ultra-trace analysis of  $^{36}\text{Cl}$  by accelerator mass spectrometry:  
 1070 An interlaboratory study. Anal. Bioanal. Chem. Res., 400, 3125–3132.  
 1071 <https://doi.org/10.1007/s00216-011-4979-2>.

1072 Moreno, P.I., Vilanova, I., Villa-Martínez, R., Dunbar, R.B., Mucciarone, D.A., Kaplan,  
 1073 M.R., Garreaud, R.D., Rojas, M., Moy, C.M., de Pol-Holz, R., Lambert, F., 2018. Onset and  
 1074 Evolution of Southern Annular Mode-Like Changes at Centennial Timescale. Sci. Rep., 8, 1–  
 1075 9. <https://doi.org/10.1038/s41598-018-21836-6>

1076 Muscheler, R., Beer, J., Kubik, P.W., Synal, H.-A., 2005. Geomagnetic field intensity during  
 1077 the last 60,000 years based on  $^{10}\text{Be}$  and  $^{36}\text{Cl}$  from the Summit ice cores and  $^{14}\text{C}$ . Quat. Sci.  
 1078 Rev., 24, 16–17, 1849–1860, <https://doi.org/10.1016/j.quascirev.2005.01.012>.

1079 Naveau, P., Jomelli, V., Cooley, D., Grancher, D. Rabatel, A., 2007. Modeling uncertainties  
 1080 in lichenometry studies with an application: The Tropical Andes (Charquini Glacier in  
 1081 Bolivia). Arct. Antarct. Alp. Res., 39, 277–288.

1082 Nichols, K. A., Goehring, B. M., Balco, G., Johnson, J. S., Hein, A. S., and Todd, C., 2019.  
 1083 New Last Glacial Maximum ice thickness constraints for the Weddell Sea Embayment,  
 1084 Antarctica. *The Cryosphere*, 13, 2935–2951, <https://doi.org/10.5194/tc-13-2935-2019>, 2019.

1085 Nicolaysen, K., Frey, F.A., Hodges, K. v., Weis, D., Giret, A., 2000.  $^{40}\text{Ar}/^{39}\text{Ar}$   
 1086 geochronology of flood basalts from the Kerguelen Archipelago, southern Indian Ocean:  
 1087 Implications for Cenozoic eruption rates of the Kerguelen plume. *Earth Planet. Sci. Lett.*,  
 1088 174, 313–328. [https://doi.org/10.1016/S0012-821X\(99\)00271-X](https://doi.org/10.1016/S0012-821X(99)00271-X)

1089 Orme, L.C., Crosta, X., Miettinen<sup>1</sup>, A., Divine, D.V., Husum, K., Isaksson, E., Wacker, L.,  
 1090 Mohan, R., Ther, O., Ikehara, M., 2021. Sea surface temperature in the Indian sector of the  
 1091 Southern Ocean over the Late Glacial and Holocene. *Clim. Past*, 16, 1451–1467.  
 1092 <https://doi.org/10.5194/cp-16-1451-2020>

1093 Park, Y.-H., Durand, I., Kestenare, E., Rougier, G., Zhou, M., d'Ovidio, F., Cotté, C., Lee,  
 1094 J.-H., 2014. Polar Front around the Kerguelen Islands: an up-to-date determination and  
 1095 associated circulation of surface/subsurface waters. *J. Geophys. Res.: Oceans*, 119, 6575-  
 1096 6592. <https://doi.org/10.1002/2014JC010061>

1097 Parnell, A.C., Buck, C.E., Doan, T.K., 2011. A review of statistical chronology models for  
 1098 high-resolution, proxy-based Holocene palaeoenvironmental reconstruction. *Quat. Sci. Rev.*,  
 1099 30, 2948e2960. <https://doi.org/10.1016/j.quascirev.2011.07.024>

1100 Pedro, J.B., Bostock, H.C., Bitz, C.M., He, F., Vandergoes, M.J., Steig, E.J., Chase, B.M.,  
 1101 Krause, C.E., Rasmussen, S.O., Markle, B.R., Cortese, G., 2015. The spatial extent and  
 1102 dynamics of the Antarctic Cold Reversal. *Nat. Geosci.*, 9, 1-6,  
 1103 <https://doi.org/10.1038/ngeo2580>.

1104 Petit, J.R., Jouzel, J., Raynaud, D., Barkov, N.I., Barnola, J.M., Basile, I., Bender, M.,  
 1105 Chappellaz, J., Davis, M., Delaygue, G., Delmotte, M., Kotiyakov, V.M., Legrand, M.,  
 1106 Lipenkov, V.Y., Lorius, C., Pépin, L., Ritz, C., Saltzman, E., Stievenard, M., 1999. Climate  
 1107 and atmospheric history of the past 420,000 years from the Vostok ice core, Antarctica.  
 1108 *Nature*, 399, 429–436. <https://doi.org/10.1038/20859>

1109 Phillips, F. M., Plummer, M. A., 1996. CHLOE: A program for interpreting in-situ cosmo-  
 1110 genic nuclide data for surface exposure dating and erosion studies. Abstracts of the 7th  
 1111 international conference on Accelerator mass spectrometry, 98–99.

1112 Phillips, F. M., Stone, W. D., Fabryka-Martin, J. T., 2001. An improved approach to  
 1113 calculating low-energy cosmic-ray neutron fluxes near the land/atmosphere interface. *Chem.*  
 1114 *Geol.*, 175, 689–701, [https://doi.org/10.1016/S0009-2541\(00\)00329-6](https://doi.org/10.1016/S0009-2541(00)00329-6).

1115 Pichon, J.-J., Labeyrie, L.D., Bareille, G., Labracherie, M., Duprat, J., Jouzel, J., 1992.  
 1116 Surface water temperature changes in the high latitudes of the southern hemisphere over the  
 1117 last glacial-interglacial cycle. *Paleoceanography*, 7, 289–318.

1118 Ponthus, L., 2018. Origine, évolution et mise en place d'un pluton récent en contexte  
 1119 intraplaque océanique. Exemple du complexe sud de Rallier du Baty, Kerguelen (T.A.A.F.),  
 1120 Ph.D. thesis, Université Toulouse 3 Paul Sabatier, France.

1121 Ponthus, L., de Saint Blanquat, M., Guillaume, D., Le Romancer, M., Pearson, N., O'Reilly,  
 1122 S.Y., Grégoire, M., 2020. Plutonic processes in transitional oceanic plateau crust: structure,  
 1123 age and emplacement in the South Rallier du Baty laccolith, Kerguelen Islands. *Terra Nova*,  
 1124 32, 408-414.

1125 Putnam, A.E., Denton, G.H., Schaefer, J.M., Barrell, D.J.A., Andersen, B.G., Finkel, R.C.,  
 1126 Schwartz, R., Doughty, A.M., Kaplan, M.R., Schlüchter, C., 2010a. Glacier advance in



1127 southern middle-latitudes during the Antarctic Cold Reversal. *Nat. Geosci.*, 3, 700–704.

1128 <https://doi.org/10.1038/ngeo962>

1129 Putnam, A.E., Schaefer, J.M., Barrell, D.J.A., Vandergoes, M., Denton, G.H., Kaplan, M.R.,

1130 Finkel, R.C., Schwartz, R., Goehring, B.M., Kelley, S.E., 2010b. In situ cosmogenic  $^{10}\text{Be}$

1131 production-rate calibration from the Southern Alps, New Zealand. *Quat. Geochronol.* 5 (4),

1132 392-409. <https://doi.org/10.1016/j.quageo.2009.12.001>.

1133 Putnam, A.E., Schaefer, J.M., Denton, G.H., Barrell, D.J.A., Finkel, R.C., Andersen, B.G.,

1134 Schwartz, R., Chinn, T.J.H., Doughty, A.M., 2012. Regional climate control of glaciers in

1135 New Zealand and Europe during the pre-industrial Holocene. *Nat. Geosci.*, 5, 1–4.

1136 <https://doi.org/10.1038/ngeo1548>

1137 Putnam, A.E., Schaefer, J.M., Denton, G.H., Barrell, D.J.A., Andersen, B.G., Koffman,

1138 T.N.B., Rowan, A.V., Finkel, R.C., Rood, D.H., Schwartz, R., Vandergoes, M.J., Plummer,

1139 M.A., Brocklehurst, S.H., Kelley, S.E., Ladig, K.L., 2013. Warming and glacier recession in

1140 the Rakaia valley, Southern Alps of New Zealand, during Heinrich Stadial 1. *Earth Planet.*

1141 *Sci. Lett.*, 382, 98-110. <http://doi.org/10.1016/j.epsl.2013.09.005>

1142 Rand, C., Goehring, B., 2019. The distribution and magnitude of subglacial erosion on

1143 millennial timescales at Engabreen, Norway. *Ann. Glaciol.*, 60(80), 73-81.

1144 <https://doi.org/10.1017/aog.2019.42>

1145 Rasmussen, S.O., Bigler, M., Blockley, S.P., Blunier, T., Buchardt, S.L., Clausen, H.B.,

1146 Cvijanovic, I., Dahl-Jensen, D., Johnsen, S.J., Fischer, H., Gkinis, V., Guillevic, M., Hoek,

1147 W.Z., Lowe, J.J., Pedro, J.B., Popp, T., Seierstad, I.K., Steffensen, J.P., Svensson, A.M.,

1148 Vallelonga, P., Vinther, B.M., Walker, M.J.C., Wheatley, J.J., Winstrup, M., 2014. A

1149 stratigraphic framework for abrupt climatic changes during the Last Glacial period based on

1150 three synchronized Greenland ice-core records: refining and extending the INTIMATE event  
 1151 stratigraphy, *Quat. Sci. Rev.*, 106, 14-28, <https://doi.org/10.1016/j.quascirev.2014.09.007>.

1152 Raup, B., Racoviteanu, A., Khalsa, S.J.S., Helm, C., Armstrong, R., Arnaud, Y., 2007. The  
 1153 GLIMS geospatial glacier database: a new tool for studying glacier change. *Glob. Planet.*  
 1154 *Change*, 56. <https://doi.org/10.1016/j.gloplacha.2006.07.018>.

1155 Reynhout, S.A., Sagredo, E.A., Kaplan, M.R., Aravena, J.C., Martini, M.A., Moreno, P.I.,  
 1156 Rojas, M., Schwartz, R., Schaefer, J.M., 2019. Holocene glacier fluctuations in Patagonia are  
 1157 modulated by summer insolation intensity and paced by Southern Annular Mode-like  
 1158 variability. *Quat. Sci. Rev.* 220, 178-187. <https://doi.org/10.1016/j.quascirev.2019.05.029>.

1159 Reynhout, S., Kaplan, M., Sagredo, E., Aravena, J., Soteres, R., Schwartz, R., Schaefer, J.,  
 1160 2021. Holocene glacier history of northeastern Cordillera Darwin, southernmost South  
 1161 America (55°S). *Quat. Res.*, 105, 1-16. <https://doi.org/10.1017/qua.2021.45>

1162 Rudolph, E.M., Hedding, D.W., Fabel, D., Hodgson, D.A., Gheorghiu, D.M., Shanks, R.,  
 1163 Nel, W., 2020. Early glacial maximum and deglaciation at sub-Antarctic Marion Island from  
 1164 cosmogenic  $^{36}\text{Cl}$  exposure dating. *Quat. Sci. Rev.*, 231.  
 1165 <https://doi.org/10.1016/j.quascirev.2020.106208>

1166 Sarıkaya, M.A., Çiner, A., Zreda, M., Şen, E., Ersoy, O., 2018. Chlorine degassing  
 1167 constrained by cosmogenic  $^{36}\text{Cl}$  and radiocarbon dating of early Holocene rhyodacitic lava  
 1168 domes on Erciyes stratovolcano, central Turkey. *J. Volcanol. Geotherm. Res.*, 369, 263-275,  
 1169 <https://doi.org/10.1016/j.jvolgeores.2018.11.029>.

1170 Schimmelpfennig, I., 2009. Cosmogenic  $^{36}\text{Cl}$  in Ca and K rich minerals: analytical  
 1171 developments, production rate calibrations and cross calibration with  $^3\text{He}$  and  $^{21}\text{Ne}$ , Ph.D.  
 1172 thesis, Université Paul Cézanne - Aix-Marseille III, France.

1173 Schimmelpfennig, I., Benedetti, L., Finkel, R., Pik, R., Blard, P.H., Bourlès, D., Burnard, P.,  
 1174 Williams, A., 2009. Sources of in-situ  $^{36}\text{Cl}$  in basaltic rocks. Implications for calibration of  
 1175 production rates. *Quat. Geochronol.*, 4, 441–461.  
 1176 <https://doi.org/10.1016/j.quageo.2009.06.003>

1177 Schimmelpfennig, I., Benedetti, L., Garreta, V., Pik, R., Blard, P.H., Burnard, P., Bourlès, D.,  
 1178 Finkel, R., Ammon, K., Dunai, T., 2011. Calibration of cosmogenic  $^{36}\text{Cl}$  production rates  
 1179 from Ca and K spallation in lava flows from Mt. Etna (38°N, Italy) and Payun Matru (36°S,  
 1180 Argentina). *Geochim. Cosmochim. Acta*, 75, 2611–2632.  
 1181 <https://doi.org/10.1016/j.gca.2011.02.013>

1182 Schimmelpfennig, I., Schaefer, J.M., Putnam, A.E., Koffman, T., Benedetti, L., Ivy-Ochs, S.,  
 1183 Schlüchter, C., Arnold, M., Aumaître, G., Bourlès, D., Keddadouche, K., 2014.  $^{36}\text{Cl}$   
 1184 production rate from K-spallation in the European Alps (Chironico landslide, Switzerland). *J.*  
 1185 *Quat. Sci.*, 29, 407–413. <https://doi.org/10.1002/jqs.2720>

1186 Schimmelpfennig, I., Schaefer, J., Lamp, J., Godard, V., Schwartz, R., Bard, E., Tuna, T.,  
 1187 Akçar, N., Schlüchter, C., Zimmerman, S. R., ASTER Team, 2022. Glacier response to  
 1188 Holocene warmth inferred from in situ  $^{10}\text{Be}$  and  $^{14}\text{C}$  bedrock analyses in Steingletscher's  
 1189 forefield (central Swiss Alps), *Clim. Past* 18, 23–44. <https://doi.org/10.5194/cp-18-23-2022>

1190 Solomina, O.N., Bradley, R.S., Jomelli, V., Geirsdottir, A., Kaufman, D.S., Koch, J., McKay,  
 1191 N.P., Masiokas, M., Miller, G., Nesje, A., Nicolussi, K., Owen, L.A., Putnam, A.E., Wanner,  
 1192 H., Wiles, G., Yang, B., 2016. Glacier fluctuations during the past 2000 years. *Quat. Sci.*  
 1193 *Rev.*, 149, 61–90. <https://doi.org/10.1016/j.quascirev.2016.04.008>

1194 Sokolov, S., Rintoul, S.R., 2009. Circumpolar structure and distribution of the Ant- arctic  
 1195 Circumpolar Current fronts: 2. Variability and relationship to sea surface height. J. Geophys.  
 1196 Res. 114 <https://doi.org/10.1029/2008JC005248>  
 1197 Stone, J.O., 2000. Isotope production. J. Geophys. Res., 105, 753–759.  
 1198 Stone, J.O., Fifield, K., Vasconcelos, P., 2005. Terrestrial chlorine-36 production from  
 1199 spallation of iron, in: Abstract of 10th International Conference on Accelerator Mass  
 1200 Spectrometry.  
 1201 Taylor, J. R., 1997. An Introduction to Error Analysis. The Study of Uncertainties in Physical  
 1202 Measurements. University Science Books, Sausalito, USA.  
 1203 Thompson, D.W.J., Solomon, S., Kushner, P.J., England, M.H., Grise, K.M., Karoly, D.J.,  
 1204 2011. Signatures of the Antarctic ozone hole in Southern Hemisphere surface climate change.  
 1205 Nat. Geosci., 4, 741–749. <https://doi.org/10.1038/ngeo1296>  
 1206 Uppala, S.M., Kållberg, P.W., Simmons, A.J., Andrae, U., Bechtold, V.D.C., Fiorino, M.,  
 1207 Gibson, J.K., Haseler, J., Hernandez, A., Kelly, G.A., Li, X., Onogi, K., Saarinen, S., Sokka,  
 1208 N., Allan, R.P., Andersson, E., Arpe, K., Balmaseda, M.A., Beljaars, A.C.M., Berg, L.V.D.,  
 1209 Bidlot, J., Bormann, N., Caires, S., Chevallier, F., Dethof, A., Dragosavac, M., Fisher, M.,  
 1210 Fuentes, M., Hagemann, S., Hólm, E., Hoskins, B.J., Isaksen, I., Janssen, P.A.E.M., Jenne,  
 1211 R., McNally, A.P., Mahfouf, J.-F., Morcrette, J.-J., Rayner, N.A., Saunders, R.W., Simon, P.,  
 1212 Sterl, A., Trenberth, K.E., Untch, A., Vasiljevic, D., Viterbo, P., Woollen, J., 2005. The  
 1213 ERA-40 re-analysis. Q.J.R. Meteorol. Soc., 131, 2961-3012.  
 1214 <https://doi.org/10.1256/qj.04.176>.  
 1215 van der Putten, N., Verbruggen, C., Björck, S., Michel, E., Disnar, J.R., Chapron, E., Moine,  
 1216 B.N., de Beaulieu, J.L., 2015. The Last Termination in the South Indian Ocean: A unique

1217 terrestrial record from Kerguelen Islands (49°S) situated within the Southern Hemisphere  
 1218 westerly belt. *Quat. Sci. Rev.*, 122, 142–157. <https://doi.org/10.1016/j.quascirev.2015.05.010>

1219 Verfaillie, D., Favier, V., Dumont, M., Jomelli, V., Gilbert, A., Brunstein, D., Gallée, H.,  
 1220 Rinterknecht, V., Menegoz, M., Frenot, Y., 2015. Recent glacier decline in the Kerguelen  
 1221 Islands (49°S, 69°E) derived from modeling , field observations , and satellite data. *J.*  
 1222 *Geophys. Res. Earth Surf.*, 120, 637–654. <https://doi.org/10.1002/2014JF003329>.

1223 Verfaillie, D., Favier, V., Gallée, H., Fettweis, X., Agosta, C., Jomelli, V., 2019. Regional  
 1224 modeling of surface mass balance on the Cook Ice Cap, Kerguelen Islands (49°S, 69°E).  
 1225 *Clim. Dyn.*, 53, 5909–5925. <https://doi.org/10.1007/s00382-019-04904-z>

1226 Verfaillie, D., Charton, J., Schimmelpfennig, I., Stroebele, Z., Jomelli, V., Bétard, F., Favier,  
 1227 V., Caverio, J., Berthier, E., Goosse, H., Rinterknecht, V., Legentil, C., Charrassin, R.,  
 1228 Aumaître, G., Bourlès, D.L., Keddadouche, K., 2021. Evolution of the Cook Ice Cap  
 1229 (Kerguelen Islands) between the last centuries and 2100 CE based on cosmogenic dating and  
 1230 glacio-climatic modelling. *Antarct. Sci.*, 33(3), 301-317.  
 1231 <https://doi.org/10.1017/S0954102021000080>

1232 WAIS Divide Project Members, 2013. Onset of deglacial warming in West Antarctica driven  
 1233 by local orbital forcing. *Nature* 500, 440–444. <https://doi.org/10.1038/nature12376>

1234 Ward, G.K., Wilson, S.R., 1978. Procedures for comparing and combining radiocarbon age  
 1235 determinations: A critique. *Archaeometry*, 20, 19–31. [https://doi.org/10.1111/j.1475-](https://doi.org/10.1111/j.1475-4754.1978.tb00208.x)  
 1236 [4754.1978.tb00208.x](https://doi.org/10.1111/j.1475-4754.1978.tb00208.x).

1237 Zreda, M.G., Phillips, F.M., Kubik, P.W., Sharma, P., Elmore, D., 1993. Cosmogenic <sup>36</sup>Cl  
 1238 dating of young basaltic eruption complex, Lathrop Wells, Nevada. *Geology*, 21, 57–60.

1239   Zweck, C., Zreda, M., Desilets, D., 2013. Snow shielding factors for cosmogenic nuclide  
1240   dating inferred from Monte Carlo neutron transport simulations. *Earth Planet. Sci. Lett.*, 379,  
1241   64-71. <https://doi.org/10.1016/j.epsl.2013.07.023>.